Structure of the Central Engine in NGC 4261 Revealed by Core Shift Measurements

A Ph.D. Dissertation Presented to
Department of Space and Astronomical Science,Graduate School of Physical Science,
The Graduate University for Advanced Studies

by
Takafumi Haga

January 23, 2014

Abstract

The compact regions in some galaxies generate a huge amount of energy and a various characteristic activities from radio thorough gamma-rays, which called active galactic nuclei (AGNs). It is widely believed that the powerful energy and activities originate from a release of gravity energy onto a super massive black hole (SMBH) from an accretion disk and this is a central engine of AGNs. The parts of energy and matter can eject in the form of jets, which have relativistic speed and emit non-thermal synchrotron. A central engine and jets are most essential components for understanding the phenomena of AGNs. However, there are some remaining problems on the black hole, the accretion disk and the jet, respectively. We do not know the position of the black hole with a sufficient accuracy, the form and the state of the accretion disk and the details of the jet mechanism such as the originating point and the form.

The main goal of this thesis is to determine the position of the black hole and to reveal the structure of the central engine and the jet mechanism. For this purpose, it is important to observe directly the location of generating the jet and the accreting the matter with the highest spatial resolution using very long baseline interferometry (VLBI). Additionally, I measure core positions with a high accuracy using multi-frequency astrometry observations and phase-referencing technique. A radio core represents the peak flux in VLBI images located at the base of jets. It appears different positions depending on frequencies, which is known as " core shift ", caused by absorption of the core emission. I select the best target source NGC 4261 for this research because it is nearby radio galaxy, has prominent two-sided jets and is a candidate of the accretion disk with sub-parsec scale.

I analyzed the core shifts to measure the core positions in both approaching and counter jet side to determine the position of the central engine in NGC 4261. The position of the core at infinity of frequency, which indicates the emission peak with no absorption, was separated by 82±16 μas from 43 GHz core position, corresponding to 310±60 $R_{\rm s}$ (Schwarzschild radius). Additionally, it is found that the core (innermost component) in counter jet side appeared to approach to the same position. I confirm for the first time that the position of the jet base is coincided with the black hole in NGC 4261. Following this determination, I investigated the structure of the accretion disk relative to the position of the black hole. Spectral index maps obtained by phase referencing technique indicate that the emission of the counter jet is affected by free–free absorption (FFA). It is consistent with the core shift profile on counter jet side because the core positions at 5–15 GHz cannot be explained for a simple synchrotron self-absorption (SSA) model. A possible solution is the SSA core shift with an additional disk-like absorber. The disk opacity profile at the counter jet side indicates the optical depth changes dramatically into optically thin at inner than the 22-GHz core position. I propose two-component structure; radiatively inefficient accretion flow (RIAF) at the inner region and a truncated disk in the outer region.

I also examined the form of the jet through the range from 10^3–10^9 $R_{\rm s}$ in NGC 4261. Using Very Large Array (VLA) data in addition to VLBA data, I measured the jet width relative to the distance from the black hole. I found that the jet shape is maintained with almost conical ($W \propto r^a$, $a = 0.91 \pm 0.03$, where W and r are the jet radius and the distance from the black hole, respectively) from parsec scale to kilo-parsec scale in outer region. This is clearly distinct from another nearby radio galaxy, M87, whose shape of the jet transitions in the region of the Bondi radius; the upstream jet maintains a parabolic shape and the downstream jet is a conical shape. Comparison of the shapes between them indicates that the jet of NGC 4261 is less accelerated while that of M87 is extremely accelerated from the modest velocity to almost light speed.

Contents

1 Introduction **1**

1.1 Overview on the Central Engine in Active Galactic Nuclei 1

1.2 Absorption at Low-Frequency Radio Band 4

1.2.1 Synchrotron Self-Absorption and Free–Free Absorption 4

1.2.2 Core Shift 6

1.3 Remained Problems on Structures the Central Engine 7

1.3.1 Position of the Black Hole 7

1.3.2 Structure of an Accretion disk 10

1.3.3 Structure of Jets 13

1.4 Aims of this Thesis 14

1.4.1 Target 14

2 Observation and Analysis **19**

2.1 VLBA Observation 19

2.1.1 Observations 19

2.1.2 Calibration and Imaging 21

2.2 VLA Observation 22

2.2.1 Observations 22

2.2.2 Calibration and Imaging 22

2.3 Measurements 24

2.3.1 Core Position 24

2.3.2 Error Estimation 24

2.3.3 Jet Width 26

3 Results **27**

3.1 CLEANed Images 27

3.1.1 Multifrequency CLEAN Images 27

3.1.2 VLA Image 29

3.2 Core Shift Measurements 30

3.3 Spectral Index Maps 34

3.4 Jet Width 37

3.5 Profile of the Jet Width 45

4 Discussion **47**
4.1 Position of the Black Hole . . . 47
4.1.1 Position of the black hole in NGC 4261 . . . 47
4.1.2 Position of the Core at 43 GHz . . . 47
4.2 What Cause the Core Shift . . . 51
4.2.1 SSA in Jets . . . 51
4.2.2 Spherical FFA Plasma . . . 51
4.2.3 SSA in Jet + FFA by the Disk . . . 52
4.3 Disk structure of NGC 4261 . . . 53
4.3.1 Disk Model . . . 53
4.3.2 Small core shift in $\nu < 2$ GHz, and $\nu > 22$ GHz . . . 54
4.3.3 Comparison of the Theoretical Model of the Transition Radius . . . 56
4.4 Jet Structure . . . 58

5 Conclusion **59**
5.1 What Are Revealed ? . . . 59
5.2 Future Prospects . . . 61

A Core Shift Theory **63**
A.1 Core Shift due to Synchrotron Self-Absorption . . . 63
A.2 Core Shift due to Free–Free Absorption . . . 65

B Details of Positional Error Estimation about Core Shift **67**

C Spherical FFA plasma model **73**
C.1 Analysis of the FFA opacity profile . . . 73
C.1.1 Core shift due to spherical FFA plasma . . . 74

Bibliography **77**

Acknowledgment **81**

List of Figures

1.1 Where is the black hole ? . . . 2
1.2 Standard disk model and RIAF model . . . 3
1.3 Combined model of RIAF and thin disk . . . 4
1.4 Spectral comparison of SSA and FFA . . . 5
1.5 Schematic illustration of the core shift of a jet . . . 6
1.6 Core shift measurements of M87 . . . 8
1.7 VLBA images at 43 GHz and proposed model of BL Lac . . . 9
1.8 Example of circumnuclear thermal plasma in pc-scales in NGC 1052 . . . 11
1.9 Example of aligning images . . . 12
1.10 Jet structure of M87 . . . 13
1.11 NGC 4261 images . . . 15
1.12 Intensity gap and its interpretation . . . 16

2.1 Very Long Baseline Array . . . 20
2.2 Positional relationship between the target source and the calibrator . . . 20
2.3 Self-calibrated image of J1222+0413 at 5 GHz . . . 21
2.4 VLA and u,v-coverage of our observation . . . 23
2.5 Contour Image of NGC 4261 using multi circular components by `modelfit` . . . 24

3.1 Self-calibrated images of NGC 4261 at every frequency . . . 28
3.2 The self-calibrated VLA image at 1 GHz . . . 29
3.3 Core positions and core shift profile . . . 31
3.4 Core shift profile of the both side jets in NGC4261 . . . 33
3.5 Spectral index maps . . . 35
3.6 Profiles of spectral index maps along jet axis . . . 36
3.7 Multi-circular Gaussian components at 1–5 GHz for the parsec scale jet . . . 40
3.8 Multi-circular gaussian components at 5–15 GHz for the parsec scale jet . . . 41
3.9 Multi-circular gaussian components at 15–43 GHz for the parsec scale jet . . . 42
3.10 The comparison between the distance from the 43 GHz core and the flux . . . 43
3.11 Self-calibrated VLA image at 1 GHz using `modelfit` in Difmap . . . 43
3.12 The profile of the jet width in NGC 4261 . . . 45

4.1 The black hole position and the innermost region of NGC 4261 . . . 48

4.2 FFA opacity profile at the counter jet side 53
4.3 Schematic illustration of our model 55
4.4 Variation of transitional radius in a truncated disk 57

5.1 Summary of this thesis 60

A.1 SSA core shift 64

B.1 Examples of `modelfit` in Difmap 70
B.2 Core identification 71

C.1 Profile of FFA opacity 74
C.2 Schematic illustration of the spherical FFA plasma model 75

List of Tables

1.1 Characteristics of disk models 3

2.1 Error budget (μas) 25

3.1 Image performance 27
3.2 Performance of VLA image 29
3.3 Core positions 30
3.4 Core shift fitting Parameters 33
3.5 Fitting parameters of the pc-scale jet (1–5 GHz) 38
3.6 Fitting parameters of the pc-scale jet (8.4–43 GHz) 39
3.7 Fitting parameters of the kpc-scale jet 44

4.1 parameters for comparison 49

C.1 The result of the parameters about the opacity profile using least-square fitting . 73

Chapter 1

Introduction

1.1 Overview on the Central Engine in Active Galactic Nuclei

Active galactic nuclei (AGNs) are compact objects at the center of galaxies, emitting huge amount of energy over the entire electromagnetic spectrum from radio through gamma rays. On the basis of their observational properties such as luminosities, optical line properties, variability and radio brightness, they are classified into some groups; Seyfert galaxies (Seyfert 1943), quasars (Greenstein & Schmidt 1964), blazers (Angel & Stockman 1980) referring to BL Lac objects (Visvanathan 1969) and optically violent variables (Cannon et al. 1971), and radio galaxies (Bolton et al. 1949). In spite of these apparent differences, it is widely believed that AGNs have the common engine, which is the release of gravitational energy from an accretion disk into a super massive black hole (SMBH) (Salpeter 1964). Energy and matter can be ejected in the form of jets, which move at relativistic velocities and emit non-thermal synchrotron radiation. In order to understand AGNs, thus, studies of the central engine, consisting of a black hole, an accretion disk and jets, are absolutely essential. Based on theoretical and observational approaches, the central engine has been extensively examined for half a century. However, some open questions still remain.

First, where is a SMBH located ? Confirming it exists in the center of a galaxy, we do not know the position of the black hole to an accuracy as the structure of the central engine. Very long baseline interferometry (VLBI), with the highest spatial resolution, is the sole technique to image the structure of central engines in AGNs. However, a VLBI image such as Figure 1.1, cannot show the black hole location uniquely; one hypothesis is the location in the close vicinity of the position of radio intensity peak, and another is predicted from the edge-brightened structure in the jet.

Second, what is the structure of an accretion disk ? What is the physical state of an accretion disk ? The typical theoretical model represents a geometrically thin and optically thick disk. This model is an analogy from the historical studies of close binary system, known as the standard accretion disk (Shakura & Sunyaev 1973). The standard disk can efficiently transfer gravitational energy into radiative energy, explaining the high-luminosity AGN successfully such as quasars (Koratkar & Blaes 1999). The spectra results in the overlap of the black body spectral

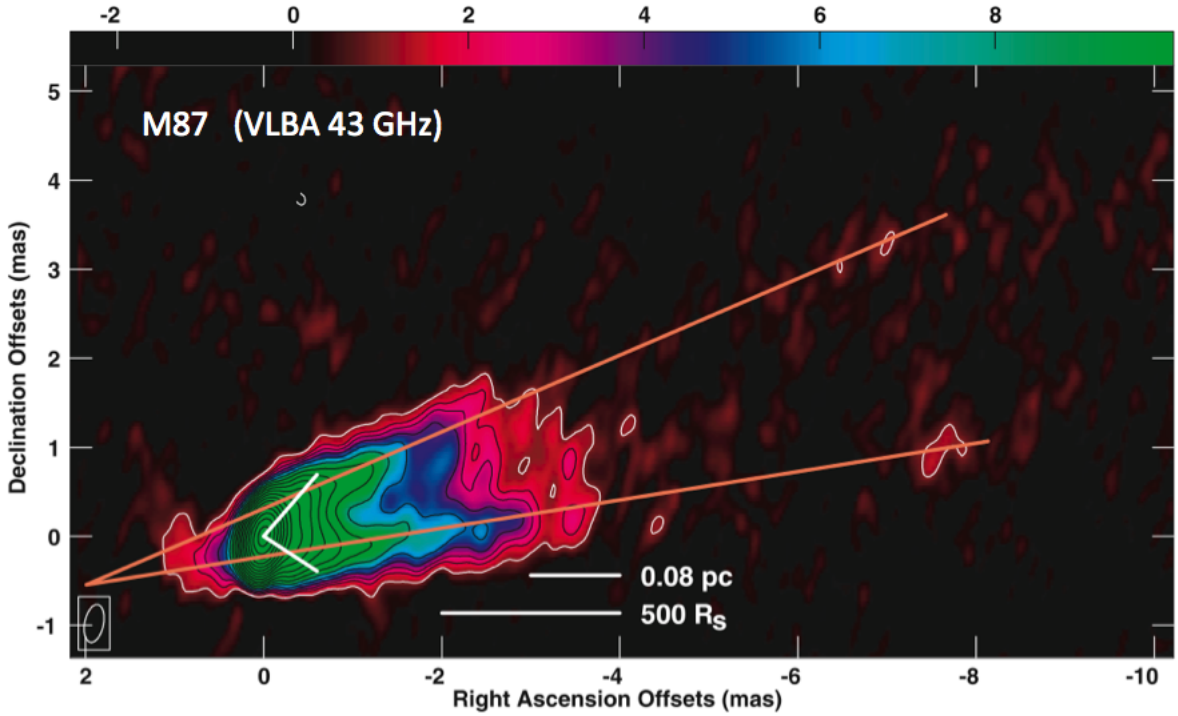

Figure 1.1: Intensity map of M87 at 43 GHz (Ly et al. 2007). The orange lines follow the edge-brightened jet emission from 10 mas west of the core, with an opening angle of 15°, while the white lines represent the wide opening angle proposed by Junor et al. (1999), indicating two possibilities of the position of the SMBH.

on various temperature and the thermal emission dominates in ultraviolet ($\sim 10^5$ K) . On the other hand, it has trouble interpreting the observational results such as the violent variability of optical emission during a short time scale ($\sim$ 1 day) and the presence of hard X-ray spectra. In this case, an alternative to the standard disk model is a geometrically thick and optically thin disk called as radiatively inefficient accretion flow (RIAF) (Yuan et al. 2003). RAIF model develop from studying the origin of Advection-dominated accretion flow (ADAF) which predicts that the structure of the flow is in some ways similar to spherical Bondi accretion (Ichimaru 1977; Narayan & Yi 1994). Since the inefficient radiation makes the accreting gas very hot, the temperature of electrons reaches $\sim 10^{9-10}$ K at close to the black hole and outflows tends to be driven. RIAF model is expected as the interpretation of low-luminosity AGNs (LLAGNs). Figure 1.2 shows the schematic of these models and I summarized the characteristics in Table 1.1. In addition, the prominent mid-IR peak and steep fall-off of the spectrum in the optical–UV region from some observations requires another model (Ho et al. 2000; Lawrence 2005; Nemmen et al. 2006).

Third, what is the mechanism of jets such as its formation, acceleration and collimation ? We do not know whether jets are formed at the black hole or the accretion disk and what kind of shape jets are. To date, the jet driving process has two established models; one is the radiative

Table 1.1: Characteristics of disk models

Characteristic	Standard disk model[a]	RIAF model[b]
Accretion rate ($\dot{m}$)	$\dot{m} \sim 1$	$\dot{m} \ll 1$
Radiation	efficient	inefficient
Optical depth (τ)	$\tau \sim 1$	$\tau < 1$
Temperature (T)	$T \sim 10^5$ K	$T \sim 10^9$ K
Geometric thickness[c] (H)	$H \ll r$	$H < r$

a: (Shakura & Sunyaev 1973) b: (Yuan et al. 2003) c: r denotes a radius of the disk

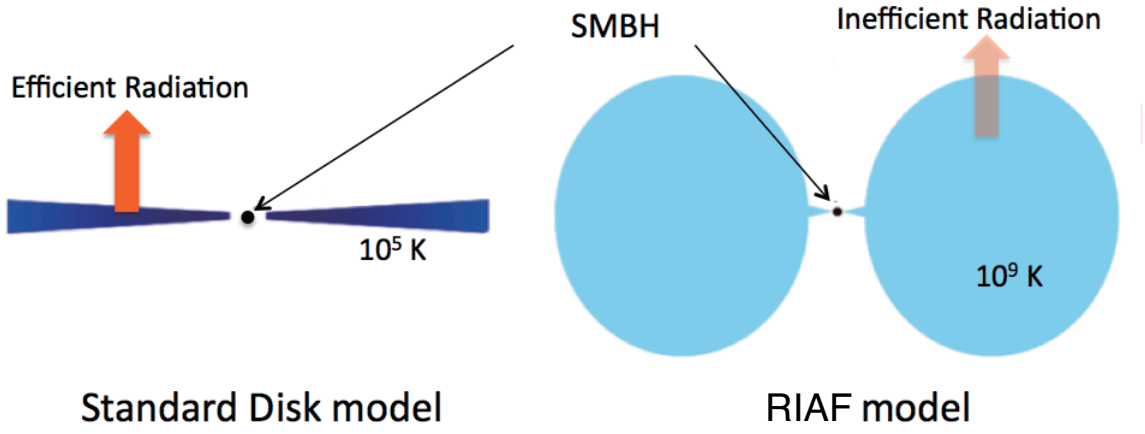

Figure 1.2: Schematic of the standard disk model (Shakura & Sunyaev 1973) and RIAF model (Yuan et al. 2003)

acceleration model (Icke 1980), and the other is the magnetohydrodynamic (MHD) acceleration model(Blandford & Payne 1982), involving deeply the formation and the collimation of jets. In the radiative acceleration model, the jet is driven by the photon pressure from the accretion disk. Icke (1980) calculated the gas flow using the standard disk model at the first time. This model can explain the spectrum of the high-luminosity AGN well because the sufficient supply of accretion matter can generate a large amount of radiation. The outward force of radiation pressure can naturally form jets and outflow against gravitational force. However, this model is not appropriate for the narrowly collimated jet because the radiation is easy to spread widely.

In contrast, MHD acceleration model can naturally explain the jet collimation, predicting that the jet is triggered by the magneto-centrifugal force (Blandford & Payne 1982). Although difficult for solving the equations of MHD dynamics, the numerical simulations indicates that the collimated jet is formed with unsteady turbulent flow (Shibata & Uchida 1990). In addition, these properties are confirmed for the general relativistic MHD simulations (Koide et al. 2002) and the recent simulation study predicts the transition of the jet structure (McKinney 2006).

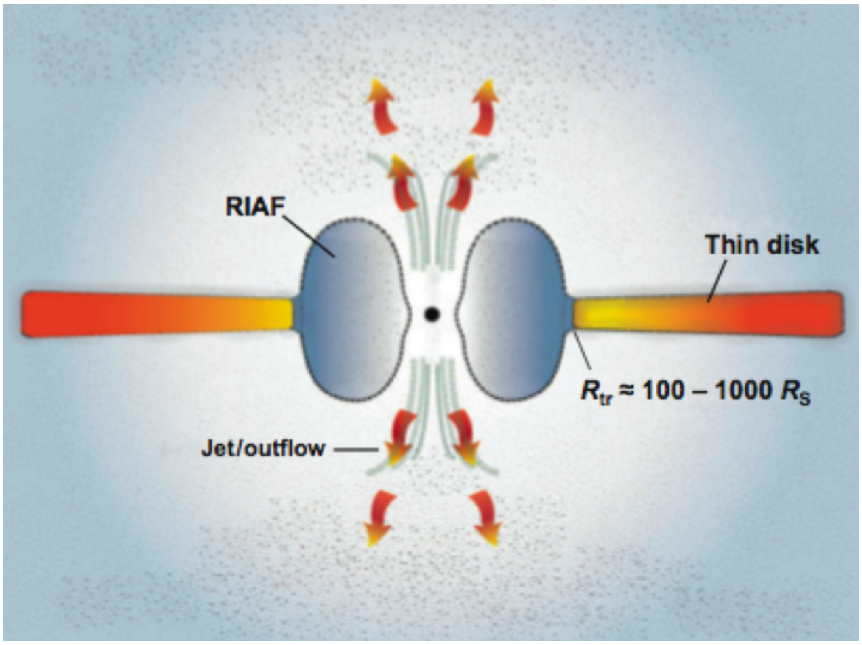

Figure 1.3: Schematic of the combined accretion model with RIAF and thin disk (Ho 2008).

However, these models of the accretion disk and the jet have been still discussed. In order to investigate three problems such as the position of the black hole, the shape and state of the accretion disk, and the mechanism of the jet, it is important to reveal the structure of the central region and relative positions of the black hole, the accretion disk, and the jet using VLBI imaging applications.

1.2 Absorption at Low-Frequency Radio Band

The non-thermal radiation of jets are mainly observed in VLBI images. On the other hand, structures of the accretion disk are estimated from the absorption in the background emission of jets. Core shifts (described below), which require to the determination of the black hole position, are also closely related to the absorption at low-frequency band. I briefly mention the processes and characteristics of the absorption at low frequency.

1.2.1 Synchrotron Self-Absorption and Free–Free Absorption

The low-frequency radio emission is absorbed for two main processes; synchrotron self-absorption (SSA), and free–free absorption (FFA). SSA is a radiative process in which the synchrotron-emitting plasma itself becomes optically thick. It is derived by a balance between the volume emissivity and the absorption coefficient of the relativistic plasma in the magnetic field. In contrast, FFA is a thermal process in which incident radiation is absorbed by a foreground plasma.

One of the major discrimination between SSA and FFA is the spectral shape at low frequency. According to textbooks for radio astronomy (e.g. Pacholczyk (1970) and Rybicki & Lightman (1979)), the spectral shape of SSA and FFA are described as

$$S_\nu = S_0 \nu^{2.5} \left[1 - \exp(-\tau_s \nu^{\alpha_0 - 2.5})\right], \tag{1.1}$$

and

$$S_\nu = S_0 \nu^{\alpha_0} \exp(-\tau_f \nu^{-2.1}), \tag{1.2}$$

where ν, S_0, α_0, τ_s and τ_f represent frequency in GHz, the flux density at 1 GHz, the spectral index of synchrotron radiation, the optical depth of SSA, and the optical depth of FFA, respectively. An example of these spectral shapes is shown in Figure 1.4. At higher frequencies than the peak frequency, the emission will be optically thin and both of the spectral index ($S_\nu \propto \nu^\alpha$) show $\alpha = \alpha_0$. At low-frequency end, the emission will be optically thick. For a SSA case, the spectral shape shows an inverted spectrum with the spectral index of $\alpha = 2.5$, independent of the frequency. On the other hand, FFA can generate steeper cutoff than the maximum attainable spectral index α of 2.5 by SSA. Thus, a component with $\alpha > 2.5$ could be an evidence of FFA.

The analysis of absorption using the spectral index distribution requires the precise astrometry and multifrequency simultaneous imaging observations. High spatial resolution is also important to avoid spectral blending for components.

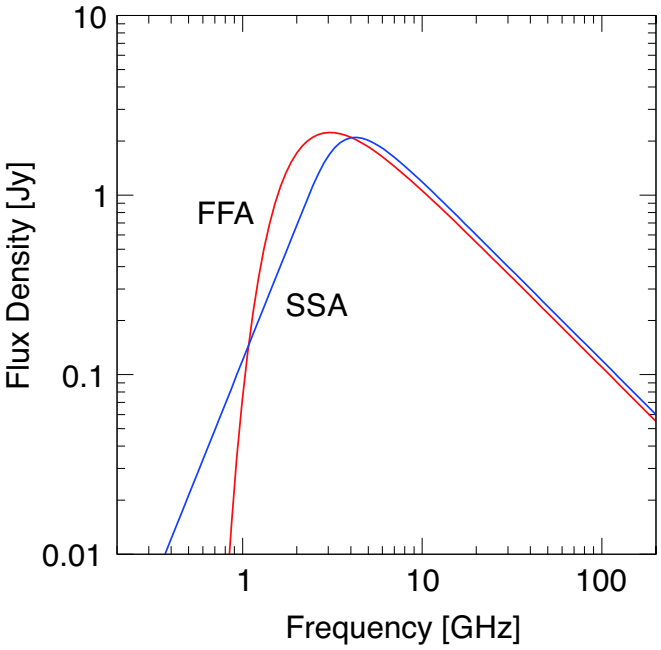

Figure 1.4: Example of comparison between the spectra of synchrotron emission with synchrotron self-absorption (blue) and free–free absorption (red)

1.2.2 Core Shift

VLBI images of AGNs often reveal a " radio core," a region of peak intensity generated by a compact unresolved component at the base of the jets. Figure 1.5 shows that the positional change of the core at different frequencies caused by the absorption of core emission , known as "core shift". The origin of the jet can be determined as a core position at infinite frequency. The absorption processes that cause core shifts are naturally SSA due to the jet itself and FFA due to the absorbing matter. Lobanov (1998) theoretically calculated the core shift on both cases (reviewed in Appendix A). According to Lobanov (1998), for the SSA case, if a jet is continuous, uniform, stationary, and travels with constant velocity, and under equipartition condition, the core position depends the frequency; that is $r(\nu) \propto \nu^{-1}$, where r and ν denotes the core position and the frequency. This type of core shift has been measured in 3C 395 (Lara et al. 1994), 3C 345 (Lobanov 1998), M81 (Bietenholz et al. 2004), among others (Sokolovsky et al. 2011). Core shifts caused by FFA depend on the size, density, and temperature of the

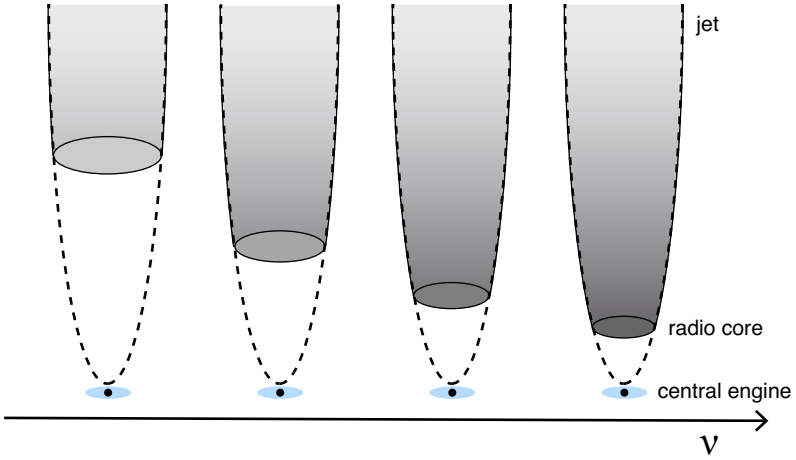

Figure 1.5: Schematic diagram explaining the core shift of a jet. The jet generated from the central engine (represented as a black dot and a blue ellipse). A radio core, defined as a region of peak intensity and a compact unresolved component at the base of the jets, is located at the unity of the opacity. The inner region of a radio core cannot be observed because of the strong absorption with $\tau > 1$. As the frequency is high, the effect of absorption is weak. Thus, cores shift towards the upper stream with increasing frequencies.

absorbing material. Thus, the frequency dependence of the FFA core shift is not determined uniquely. Previous observational studies have very little clear evidence about FFA core shifts, except a few examples indicating the possibility of them (e.g. Cyg A (Krichbaum et al. 1998) and NGC 1052 (Kadler et al. 2004)).

1.3 Remained Problems on Structures the Central Engine

High resolution studies such as VLBI observations have revealed the structure of the central region. I provide the latest studies and remained problems on each component in the central engine.

1.3.1 Position of the Black Hole

Assuming that the origin of the jet coincident with the black hole position, the position of the central engine can be determined as the core position at infinite frequency. Hada et al. (2011) estimated the accurate position of the central engine of M87 by measuring the core shifts using multifrequency and phase-referencing (Figure 1.6) for the first time.

In the case of M87, the black hole is located 23 $R_{\rm s}$ distant from the observed core at 43 GHz, assuming that the asymptotic line, representing the origin of a jet, spatially coincides with the black hole. The core shift of M87 was fitted well with $\propto \nu^{-0.94}$, supporting that the absorption process is interpreted as SSA of the jet.

Figure 1.7 shows, on the other hand, the radio cores of blazers or BL Lac objects (hereafter termed BL Lac) manifest as standing shock points up to 10^4–10^6 $R_{\rm s}$ distant from the black hole (Jorstad et al. 2001, 2005; Marscher et al. 2008). The core location in the BL Lac is actually 10^4–10^6 $R_{\rm s}$ from the black hole, as determined from γ-ray monitoring observations (Albert et al. 2007).

Two different case indicate fuzziness of the connection between the limiting core position and central engine location. Whether this fuzziness really exists is not easily determined, because most core shift measurements have been performed on single-sided jet sources. Although core shift measurements in counter jets have been attempted (Kadler et al. 2004), these are rendered inaccurate because of the lack of the accuracy to overlap more than two images without phase-referencing observations.

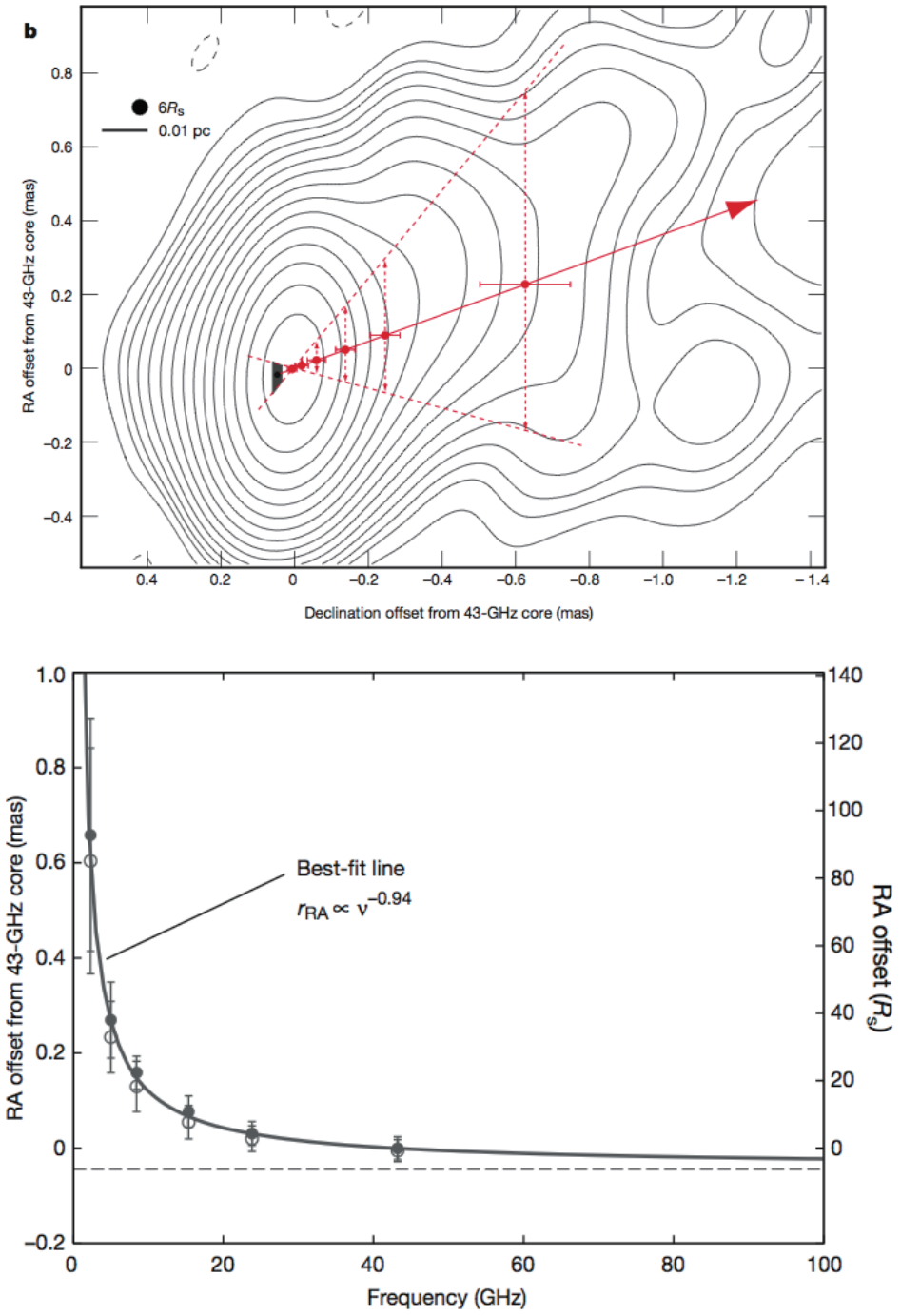

Figure 1.6: Core shift measurements of M87 (Hada et al. 2011). (Top) VLBA image of M87 at 43 GHz. Red crosses and the shade area denote the measured core shift positions and the origin of the jet, respectively. (Bottom) Plot of the core positions in right ascension as a function of observing frequency. The solid curve represents the best-fit solution, close to the asymptotic line which is located at 41 ± 12 μas eastwards from the 43 GHz core. It is equivalent to the projected separation 6 ± 2 $R_{\rm s}$ for the black hole mass $M = 6 \times 10^9 M_\odot$ and the distance of 16.7 Mpc.

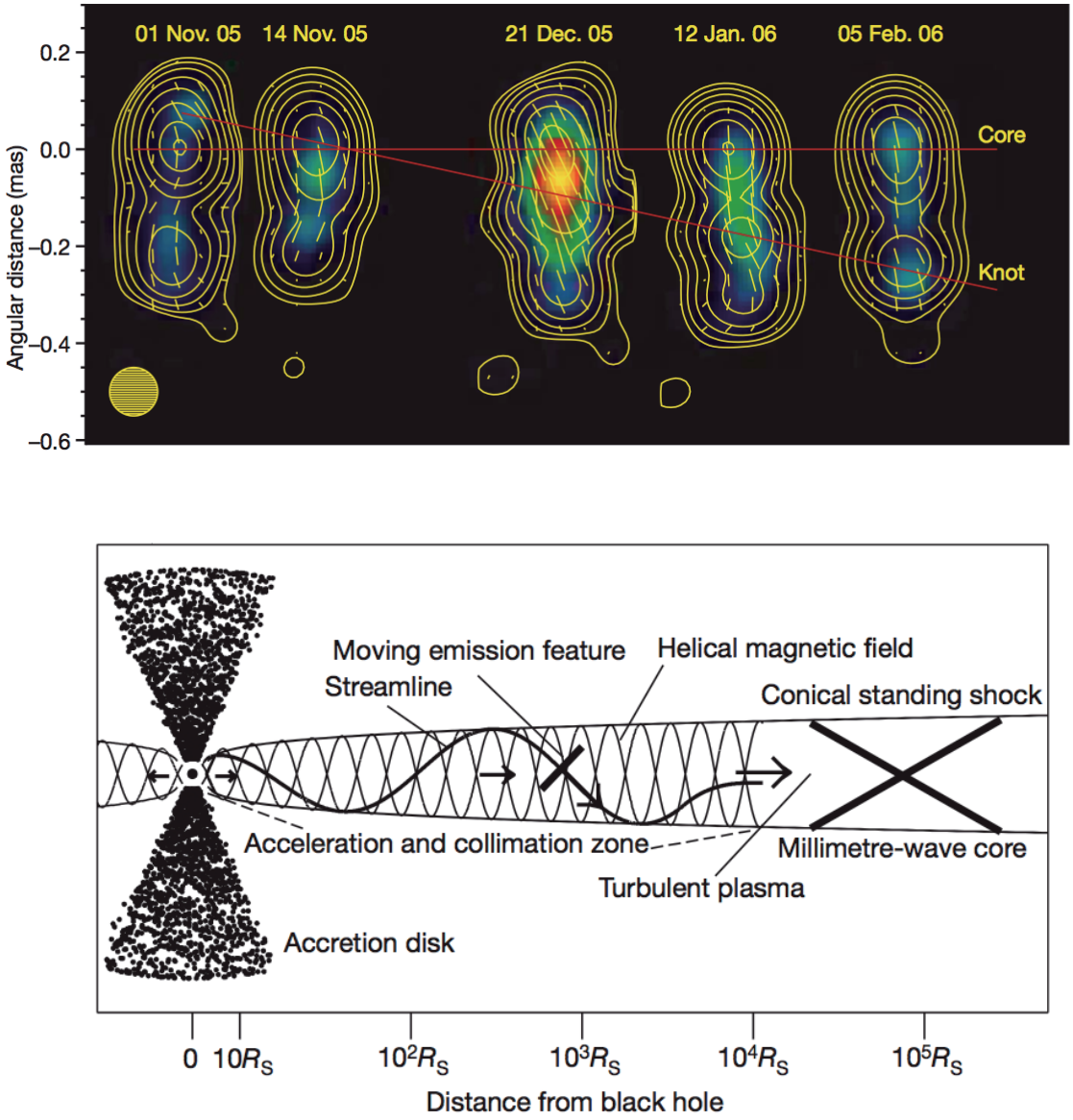

Figure 1.7: VLBA images at 43 GHz and proposed model of BL Lac (Marscher et al. 2008). (Top) Sequence of Very Long Baseline Array images of BL Lac at 43 GHz. The contours and the color scale represents total flux intensity and polarized intensity. The yellow line segments indicate the electric vector position angle (EVPA) of the polarization. The EVPA has been rotated in the clockwise direction to compensate for Faraday rotation. The approximate path of the centroid of the knot, the definition of which includes a point from an image obtained on 12 March 2006, is given by the slanted red line.
(Bottom) Plot of the core positions in right ascension as a function of observing frequency. A shock propagates down the jet along a spiral streamline. The first flare occurs before the flow straightens and becomes turbulent. The passage of the feature through the millimeter-wave core stimulates the second flare. A logarithmic scale of distance from the black hole, shown in terms of the Schwarzschild radius (R_s), is used to illustrate phenomena on various scales.

1.3.2 Structure of an Accretion disk

Circumnuclear thermal plasma in parsec scales are a promising candidate of reservoir to fuel material to inner accretion disk. Spectral indices of $\alpha > 2.5$, which cannot be attributed to SSA but FFA, are found near the nuclei at ~ 1 pc. The structure of the accretion disk is estimated from the distribution of the jet absorption. In fact, a wide variety of these structures has been suggested in some objects: e.g., geometrically thin disk (NGC 4261; Jones et al. 2001), torus (NGC 1068; Gallimore et al. 1997, NGC 1052; Kameno et al. 2001, 3C 84; Walker et al. 1994, Cyg A; Conway & Blanco 1995), and spherical structures (OQ 208; Kameno et al. 2000). Figure 1.8 shows an example of the structure predicted by the distribution of absorption. The accurate distribution of a spectral index requires an appropriate reference position when overlaying images at different frequencies. The core position is frequently assumed as the reference position for each frequency image; however, as discussed above, this moves with frequency change because of absorption, producing inaccurate spectral index maps. Many previous studies did not perform properly, except for using opacity-thin jet components as reference positions (Kameno et al. 2001). An example of the alignment in previous studies is shown in Figure 1.9. The method of utilizing the feature of the jet intensity could lead to the ambiguity of the alignment. Furthermore, the core shift mechanism (FFA and/or SSA) cannot be precisely identified in the absence of spectral index information.

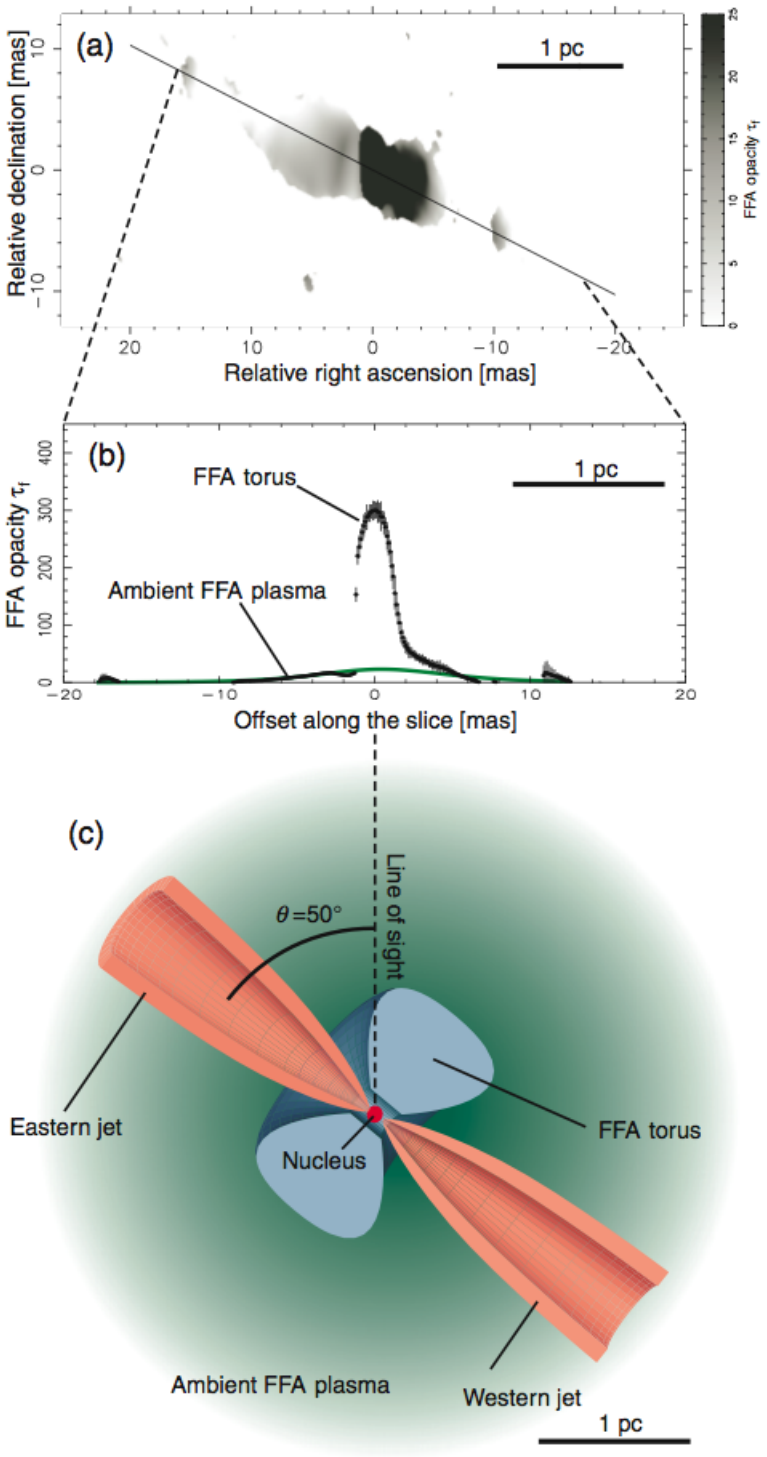

Figure 1.8: Distribution of the FFA opacity and a schematic model of a torus surrounding NGC 1052. (a): The distribution of the FFA opacity is drawn in gray scale. (b): The opacity profile along the jet in P.A. =65°. It described by the best-fit models of the FFA tours and the ambient FFA plasma. (c): A schematic diagram of NGC 1052. In this study, opacity-thin jet components were used as reference positions to obtain the accurate distribution of absorption.

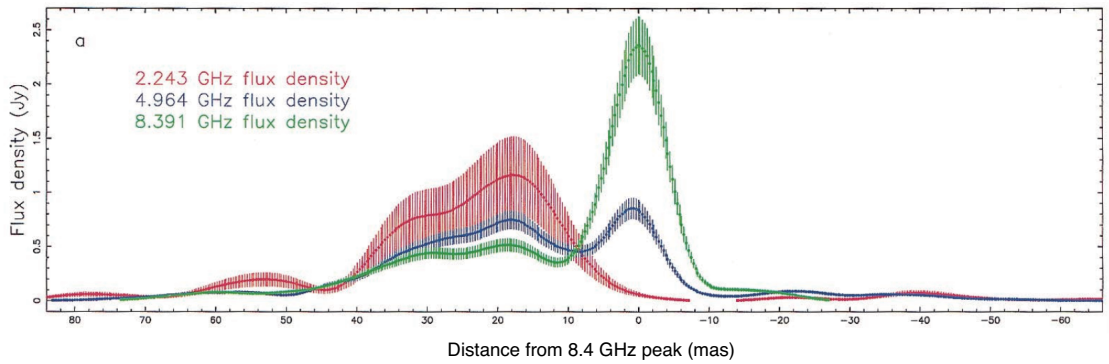

Figure 1.9: Example of aligning images at different frequencies for spectral index distribution (Tingay & Murphy 2001). At first, the alignment between 8.4 and 5.0 GHz was proceeded using the features in the bright part of the jet. Next, the 2.2 and 5.0 GHz images were registered in the same way. However, the ambiguity of the alignment remains because the core shift is unconsidered.

1.3.3 Structure of Jets

Recently, some VLBI observations with a high spatial resolution revealed directly the structure at an innermost region of the jet. Asada & Nakamura (2012) found that the M87 jet maintains a parabolic streamline between a few 100 R_s and 10^5 R_s and then transitions from a parabolic into a conical shape farther downstream (Figure 1.10). This indicates that the MHD jet is confined by the external interstellar medium (ISM) pressure at a parabolic region and the jet freely expands at a conical region. The transition was interpreted as the changing profiles of the external pressure at Bondi radius. Furthermore, Hada et al. (2013) revealed a collimation profile down to 10 R_s of the M87 jet. As close to the black hole, the jet showed a possibility of the slightly steeper shape than parabolic streamline at the outer jet, consistent with the model predicted by relativistic MHD jet. The investigation of other sources is significantly important because the comparison of the jet structure in the innermost region helps to close in the details of the processes. However, the application of this approach for other sources has not been progressed yet because of the lack of information of the black hole position.

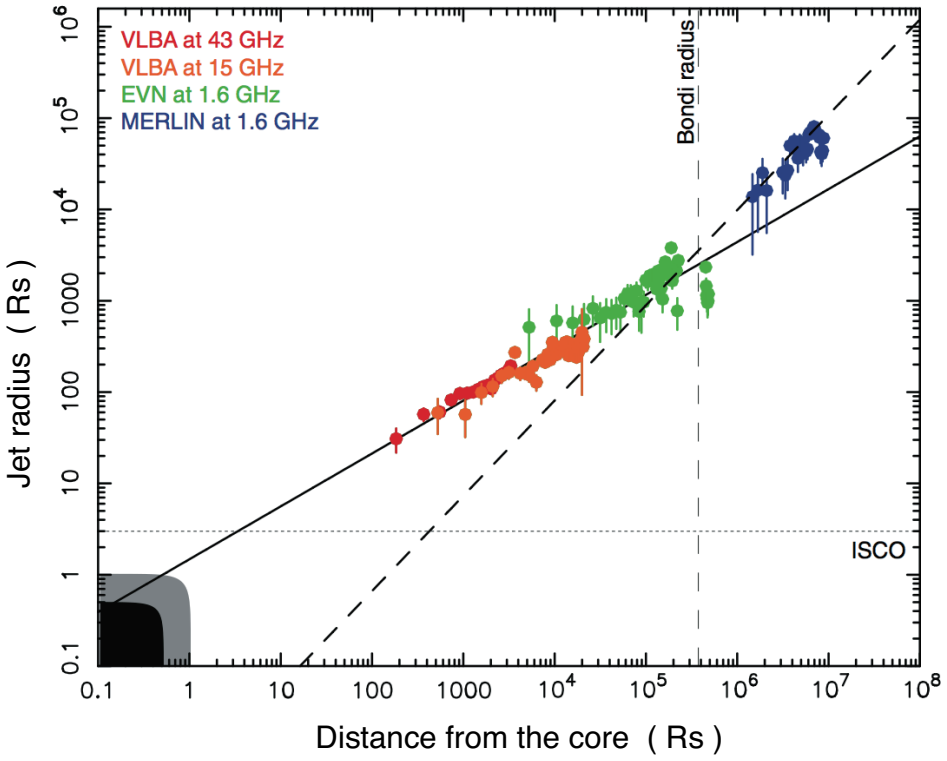

Figure 1.10: Distribution of the radius of the jet as a function of the de-projected distance from the core in units of R_s. The jet is described by two different shapes. The solid line indicates a parabolic structure with a power-law index ($W \propto r^a$), a of 0.58, while the dashed line indicates a conical structure with a of 1.0, where r and W is the width of the jet emission and the axial distance from the core. HST-1 is located around 5×10^5 R_s. The black area shows the size of the minor axis of the event horizon of the spinning black hole with maximum spin. The gray area indicates the size of the major axis of the event horizon of the spinning black hole with maximum spin, and corresponds to the size of the event horizon of the Schwarzschild black hole. The dotted line indicates the size of the inner stable circular orbit (ISCO) of the accretion disk for the Schwarzschild black hole.

1.4 Aims of this Thesis

Main goal of this thesis is to reveal the structure of the central engine and the jet mechanism in AGNs based on VLBI imaging and very accurately determining the position of black hole. It is important to observe directly the location of generating the jet and the accreting the matter with the highest spatial resolution using VLBI. Additionally, I measure core positions with a high accuracy using multifrequency astrometry observations and phase-referencing technique. I select the best target source NGC 4261 for this research because it is nearby radio galaxy, has prominent two-sided jets and is a candidate of the accretion disk with sub-parsec scale.

1.4.1 Target

NGC 4261 (3C 270) is one of the nearby Fanaroff-Riley Class I (FR-I) radio galaxy. The galaxy is 31.6 Mpc distant from the Earth (Tonry et al. 2000), corresponding to 0.15 pc/mas. This proximity presents an advantage for studying regions within 1 pc of the central engine. Based on Very Large Array (VLA)(Thompson et al. 1980 observations, the large scale jet was revealed, indicating about 35 kpc jet with extended and faint lobe at each side. The jet at both side extends straight with an opening angle of less than 5° out to 5 kpc from the nucleus(Birkinshaw & Davies 1985). The nucleus of NGC 4261 is known to contain a central black hole with a mass of $(4.9 \pm 1.0) \times 10^8\ M_\odot$ (Ferrarese et al. 1996). Hubble Space Telescope (HST) observations have also revealed a disk of gas and dust, having a diameter of 300 pc, in the NGC 4261 nucleus (Jaffe et al. 1993). Another feature of NGC 4261, revealed by VLBI studies, is its prominent two-sided jet with parsec-scale along large-scale jets, running parallel to the rotation axis of the dust disk (Jones et al. 2000). The West- and East-side jets are approaching and receding to observers, respectively; the latter is known as a counter jet. The brightness of both jets is slightly affected by relativistic beaming. Piner et al. (2001) estimated the speed of the jets by very long baseline array (VLBA) monitor observations at 8 GHz. From the jet-to-counter jet brightness ratio and apparent speed, they obtained a gentle intrinsic jet velocity of about $(0.46 \pm 0.02)c$, inclined at $63 \pm 3°$ from the line of sight. However, the structure of the jet in this scale has not been investigated yet. In addition, the two-sided jet of NGC 4261 is also advantage to compare the physical conditions between the approaching and the counter jet.

NGC 4261 is further characterized by an apparent discontinuity in the structure of the counter jet. This region, called the "gap", has been interpreted as obscuration by an edge-on, geometrically thin, cold parsec-scale disk with a temperature of $\sim 10^4$ K (Jones et al. 2001). As an alternative to the FFA disk model, the gap may arise from resistive radiatively inefficient accretion flow (Kaburaki et al. 2010). According to Kaburaki et al., the low temperature of the standard disk model (Shakura & Sunyaev 1973) precludes the existence of FFA plasma gas in a gap region so distant from the central black hole.

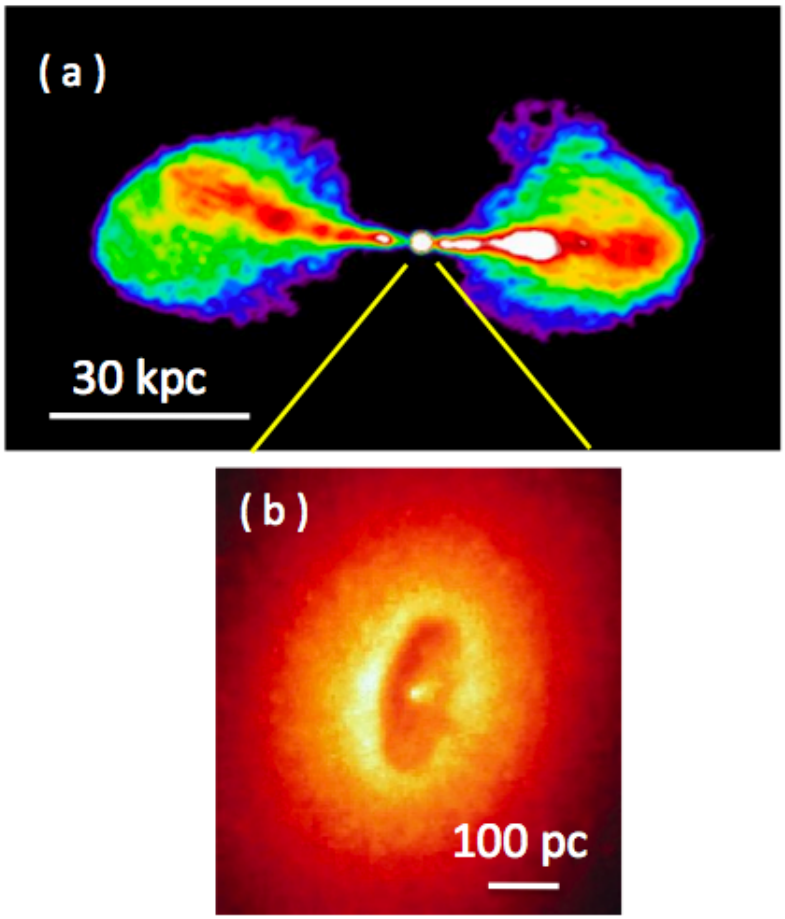

Figure 1.11: Images of NGC 4261 on different scales. (a): VLA observation of NGC 4261(Condon & Broderick 1988). Symmetric large scale two-sided jets was extended about 35 kpc with faint lobe at each side. (b): HST observation of NGC 4261(Jaffe et al. 1993). A disk of gas and dust has a diameter of 300 pc in the NGC 4261 nucleus.

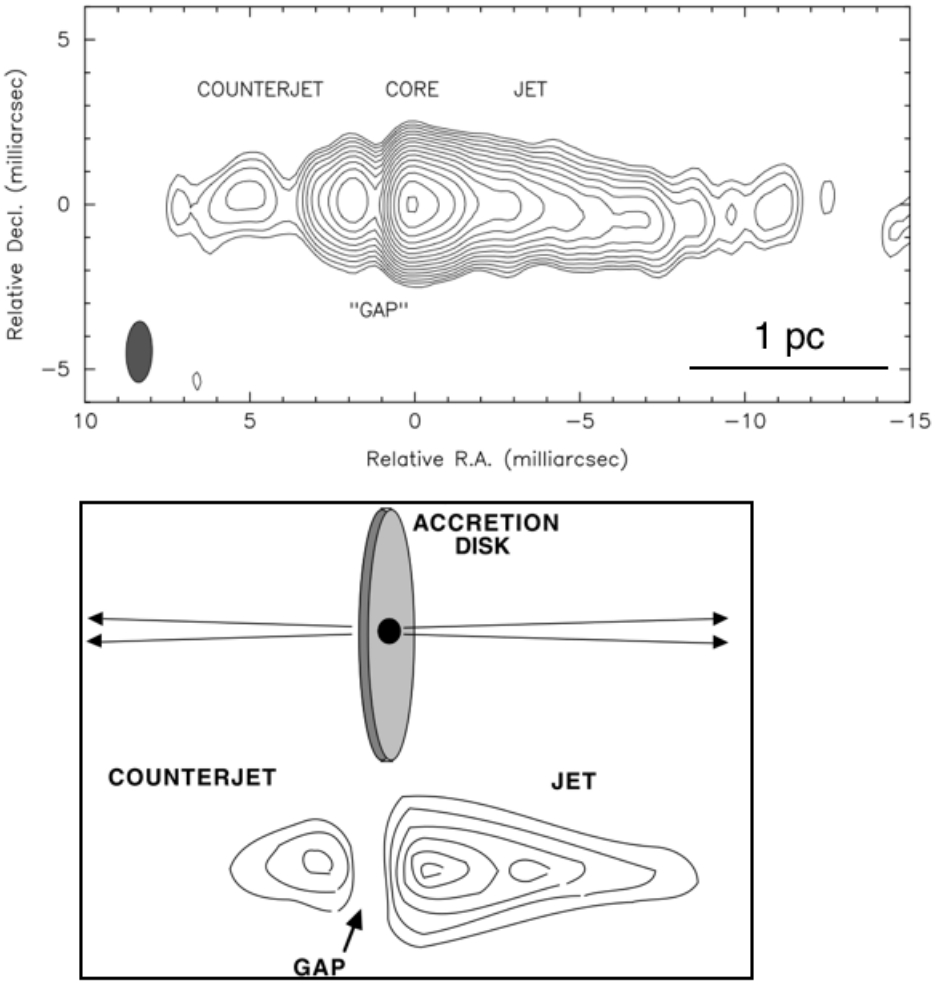

Figure 1.12: (Top) VLBA image of NGC 4261 at 8.4 GHz (Jones et al. 2001). One in west side is an approaching jet and another in east side is a receding, counter jet. The apparent discontinuity ("gap") is located on the counter jet, close to position of the peak intensity (core).
(Bottom) A proposed disk model (Jones et al. 2000). The narrow gap was interpreted as the obscuration by edge-on, geometrically thin, cold and parsec scale disk with the temperature of $\sim 10^4$ K.

This thesis is organized as follows. In section 2, I describe details of the observation and analysis. In section 3, I show the main results obtained from the core shift measurements, spectral index maps and the jet width measurements. In section 4, I discuss the nature and geometry of the central engine in NGC 4261. Section 5 describes the main conclusions.

Chapter 2

Observation and Analysis

2.1 VLBA Observation

2.1.1 Observations

Multi-frequency observations of NGC 4261 were conducted using the VLBA (Napier 1994) at four frequency bands (1.4, 2.3, 5.0, and 8.4 GHz) on July 3, 2003, and at three frequency bands (15, 22, and 43 GHz) on June 26, 2003. The two sets of observations were separated by only 7 days. Each observation period was approximately 12 h. At 1.4 GHz, dual-circular polarization at two intermediate frequencies (IF) were received, covering a total bandwidth of 16 MHz. At both 2.3 and 8.4 GHz, two IFs covered a total bandwidth of 16 MHz in right-hand circular polarization. Other frequency bands collected four IFs, covering a total bandwidth of 32 MHz in left-hand circular polarization. 2-bit sampling was applied at all observational frequency bands. Correlations were processed using the VLBA correlator in Socorro, New Mexico.

The radio core positions of NGC 4261 were measured by the nodding-style phase-referencing technique, relative to a nearby reference source, J1222+0413, separated within 2° of NGC 4261; ⋯-T-C1-T-C1-T-⋯, where T and C1 represent the target and primary calibrator, respectively. Figure 2.2 shows the positional relationship between them on the celestial sphere. Switching between the target and calibrator was repeated after scanning for 20 s. Observations were conducted for approximately 20 min at each frequency in turn. Under this measurement condition, the (u,v)-coverage among frequencies was almost identical, thereby minimizing the residual systematic errors in astrometry. The total on-source time on the target was approximately one hour at each frequency.

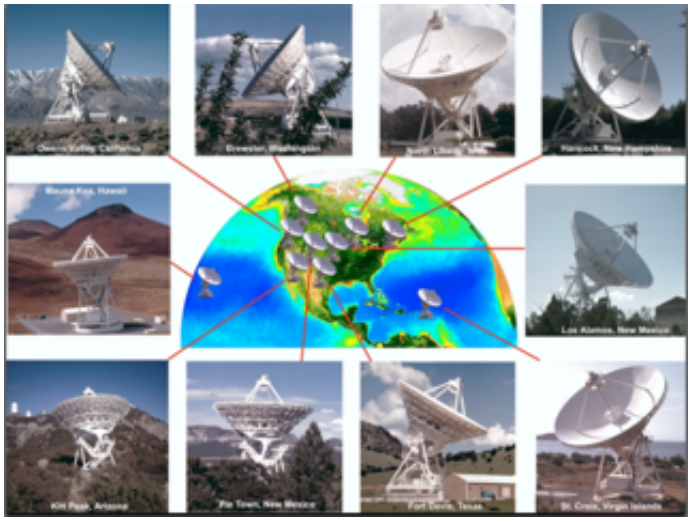

Figure 2.1: The VLBA is an interferometer consisting of ten 25-m-diameter antennas, one is the U.S. virgin Islands, eight in the continental United States, and one in Hawaii (Napier, 1994). Each telescopes are separated by distance ranging from 200 km to 8600 km.

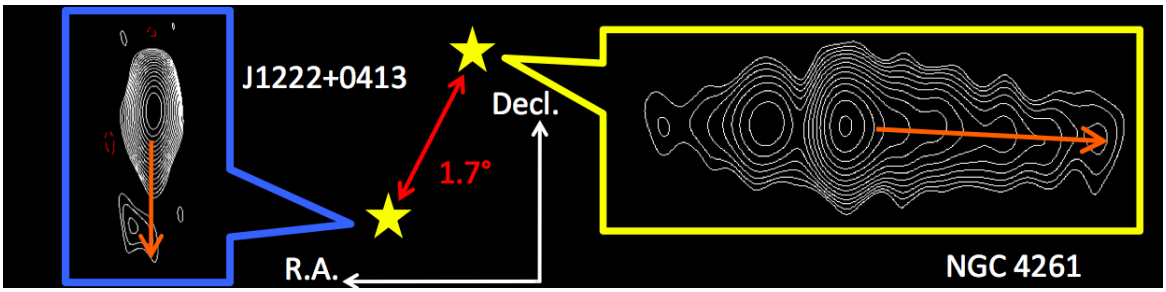

Figure 2.2: Positional relationship between NGC 4261 and J1222+0413 on the celestial sphere. They are separated with 1.7°. Contour maps and orange arrows represent self-calibrated images provided by CLEAN algorithm and the direction of the jets. The jet directions are nearly perpendicular, which is important to measure the core shift (for details, see Section 3.2).

2.1.2 Calibration and Imaging

The antenna parallactic angles, Earth orientation parameters, and ionospheric dispersive delays were corrected using the ionospheric model from GPS data provided by the Jet Propulsion Laboratory (Mannucci et al. 1999). Instrumental delays/phases and bandpass were calibrated using 3C 273 data. Assuming a point source model, we performed fringe-fitting on J1222+0413 as a phase calibrator C1. Subsequently, we corrected the amplitude and phase parameters using a source structure model available in the Difmap software (Shepherd et al. 1994). This model is based on iterative deconvolution and self-calibration algorithms. Applying these solutions to the visibilities of NGC 4261, we obtained phase-referenced images of NGC 4261.

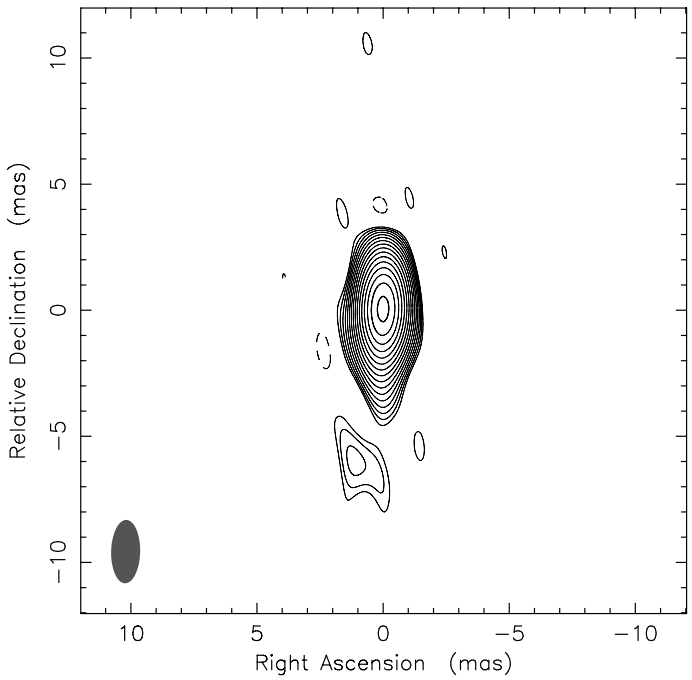

Figure 2.3: Self-calibrated image of J1222+0413, collected at 5 GHz. The jet extends to the South, almost perfectly perpendicular to the jet of NGC 4261.

2.2 VLA Observation

2.2.1 Observations

We analyzed the archival VLA data (AJ229) from the data archive system of the National Radio Astronomy Observatory (NRAO). This observation were conducted on 1994 April 15–16 at 1.4 GHz (L-band) while in its A-configuration with 27 antennas. Dual-circular polarization were received, covering a bandwidth of 3 MHz. In the 6.5 hr observing run, the total on-source time on the target was approximately 5.5 hr and 3C286 was observed as the calibrator for 1 hr. Figure 2.4 show u,v-coverage of VLA observation.

2.2.2 Calibration and Imaging

Data reduction was performed in the ordinary manner using AIPS. The primary flux, the amplitudes and phase were calibrated using 3C 286. We interpolate the solution derived from the calibrator into the target. After the data were averaged over 30 s, we performed iterative deconvolution and self-calibration algorithms using Difmap. Then, we finally obtained the self-calibrated image.

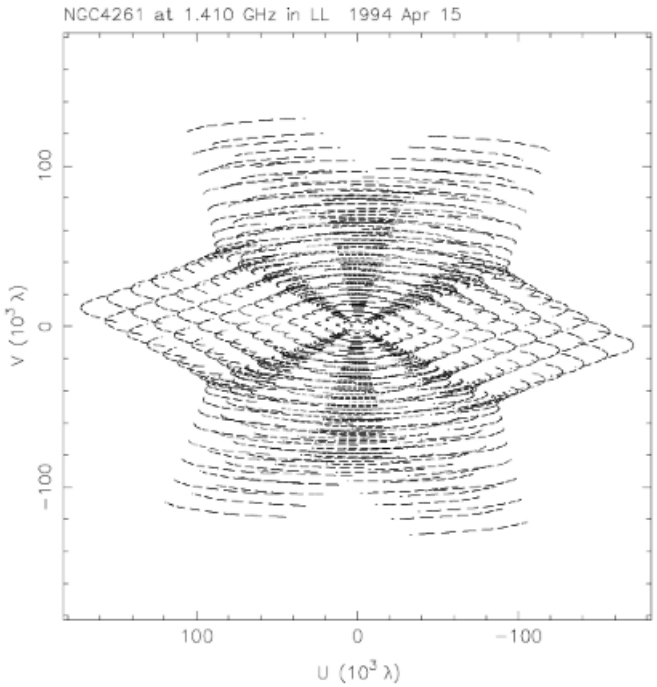

Figure 2.4: (Top): The Very Large Array (VLA) consists of 27 radio antennas in a Y-shaped configuration on the Plains of San Agustin fifty miles west of Socorro, New Mexico. Each antenna is 25 meters in diameter. (Bottom): u,v-coverage of our observation with A–configuration during 5.5 hour.

2.3 Measurements

2.3.1 Core Position

The source position in the phase-referenced images was measured using `JMFIT` in AIPS (Greisen 2003), adopting a single-ellipse Gaussian profile model. However, we consider that, because the core and jets were blended, the core position drifted slightly toward the jet side from its true position. The jet contribution was estimated by comparing two methods of measuring the core position in final images; one-component `JMFIT` and fitting of visibility data to multi circular Gaussian components using `modelfit` in Difmap (Figure 2.5). The methods were iteratively performed on CLEAN and self-calibration images. The final core position was defined as the position measured in phase-referenced images, corrected for the jet contribution.

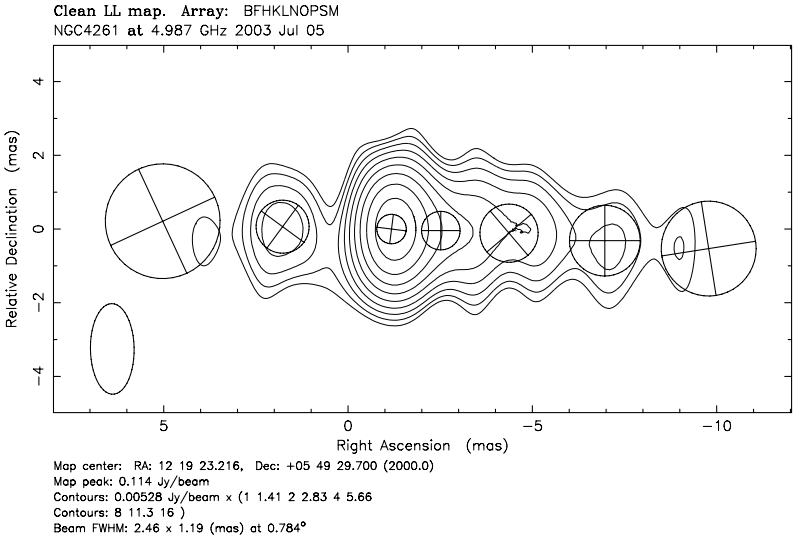

Figure 2.5: Contour image of NGC 4261at 5 GHz and multi-circular components by `modelfit` in the Difmap.

2.3.2 Error Estimation

Following the method of Hada et al. (2011), I estimated the error in my astrometric measurements. The error incorporates ionospheric residuals, tropospheric residuals, antenna positional error, Earth orientation error, a priori source coordinate error, core identification error, and thermal noise. The error contributions are listed in Table 2.1. Based on GPS data, I assume a total electron content of $3 \times 10^{17}\mathrm{m}^{-2}$, reducible to 1/4 equivalent following ionospheric residual correction by `TECOR` (Mannucci et al. 1999). The zenith excess path error in tropospheric residuals is 2 cm (Beasley & Conway 1995). I adopted proper geometric errors such as antenna error (3 mm), Earth orientation error (VLBA memo 69), and a priori source coordinate error, determined from source declination (Pradel et al. 2006). The core identification error was estimated from the difference in core positions yielded by the above-described fitting methods. The thermal noise error was defined by the beam size over the dynamic range of phase-referenced maps. More detailed information is described in Appendix B.

Table 2.1: Error budget (μas)

Frequency [GHz]	1.4	2.3	5.0	8.4	15	22	43
Phase-referencing observation							
Beam width/ signal to noise	52	24	10	6	4	3	2
Ionosphere	2006	779	161	57	17	8	2
Troposphere	13	13	13	13	13	13	13
Earth orientation	5	5	5	5	5	5	5
Antenna position	2	2	2	2	2	2	2
Apriori source coordinates	1	1	1	1	1	1	1
Core identification analysis							
A-Jet	349	60	17	40	3	5	3
C-Jet	343	26	5	50	326	312	19
Total error (RSS)							
A-Jet	2055	792	170	77	30	23	19
C-Jet	2054	790	169	82	328	313	25

2.3.3 Jet Width

In previous studies of M87, Asada & Nakamura (2012) analyzed the jet emission along the direction perpendicular to the jet and fitted the cross section mainly two Gaussians. Thus, they defined the distance between the outer edges of the two FWHMs as the width of the jet. This definition represents jet width successfully because M87's jet has the edge-brightened structure. On the other hand, I do not know that this definition is appropriate for NGC 4261 since such a structure is not appeared. Therefore, the jet width was measured using `modelfit` in Difmap to fit visibility data by multi-circular gaussian components in final images. I define the width of the jet as FWHM of the circular gaussian components. When fitting visibility, I set the position, the flux density, and the FWHM radius of each component as free parameters.

Chapter 3

Results

3.1 CLEANed Images

3.1.1 Multifrequency CLEAN Images

Figure 3.1 shows the (self-calibrated) CLEANed images, uniformly weighted at each frequency. The beam sizes and image qualities are listed in Table 3.1. Approaching jets and counter jets, extending West and East from the brightest region (core), appear in the images at $\leq$ 15 GHz. The counter jet is not prominent in the image recorded at 22 GHz, while no obvious jet-like structures are visible in the 43 GHz image. However, both approaching and counter jets appear in the model components of `modelfit` in Difmap. The lower the frequency, the more extended and symmetric the jets.

Table 3.1: Image performance

ν (GHz) (1)	$I_{\rm peak}$ (mJy/beam) (2)	σ (mJy/beam) (3)	$\theta_{\rm maj}$ (mas) (4)	$\theta_{\rm min}$ (mas) (5)
1.4	47.4	0.50	8.90	4.45
2.3	70.1	0.69	5.41	2.60
5.0	117.1	0.58	2.47	1.19
8.4	101.6	0.60	1.51	0.69
15	113.4	0.71	0.85	0.37
22	123.2	1.27	0.55	0.27
43	72.9	0.94	0.30	0.16

Columns are as follows: (1) Frequency; (2) Peak intensity; (3) Image RMS noise; (4) The major axis size of the synthesized beam; (5)The minor axis size of the synthesized beam

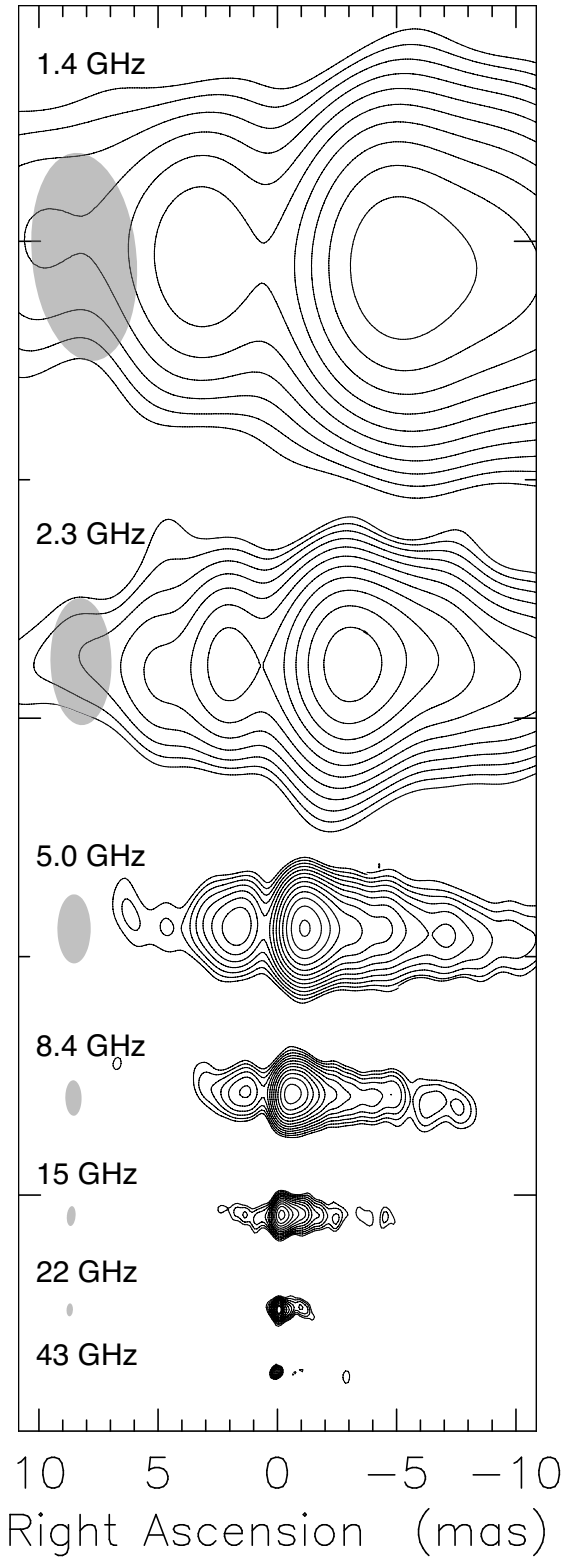

Figure 3.1: Self-calibrated images of NGC 4261 at each observation frequency, aligned relative to the 43 GHz core (accounting for core shifts). The gray ellipses show the synthesized beam size (FWHM). The RMS noise in the images at each frequency is provided in Table 3.1. Contours start at the $\pm 3\sigma$ level, increasing by factors of $\sqrt{2}$.

3.1.2 VLA Image

Figure 3.2 shows the (self-calibrated) CLEANed image of the kpc-scale jet with restored beam. The image characteristic is provided in Table 3.2 The approaching jet and the counter jet extend 120 arcsec West and 150 arcsec East (25 arcsec $\sim$ 4 kpc) from the brightest region. The counter jet slightly bends from East to North and has the weak emission at 20 arcsec North. Compared to the approaching jet, the counter jet are weak and blobby.

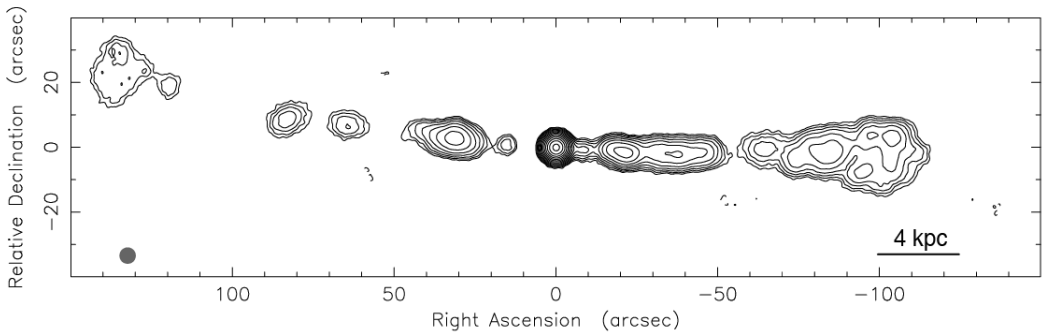

Figure 3.2: The self-calibrated VLA images of NGC 4261 at 1.4 GHz. The gray circle show the restored beam size (FWHM) with 5 arcsec. The RMS noise in the images is 0.52 mJy/beam. Contours start at the $\pm 3\sigma$ level, increasing by factors of $\sqrt{2}$.

Table 3.2: Performance of VLA image

ν	$I_{\rm peak}$	σ	$\theta_{\rm R}$
(GHz)	(mJy/beam)	(mJy/beam)	(arcsec)
(1)	(2)	(3)	(4)
1.4	159.2	0.52	5

Columns are as follows: (1) Frequency; (2) Peak intensity; (3) Image RMS noise; (4) The size of the restored beam

3.2 Core Shift Measurements

The core positions measured in phase-referenced images of NGC 4261 at 1.4–43 GHz are plotted on the 5 GHz self-calibrated image in Figure 3.3. The core appears to shift northwestward as the frequency decreases. The jet of the reference source J1222+0413 is oriented nearly perpendicular to that of NGC 4261 (toward the South, whereas the NCG 4261 jet tends to the West; see Figure 2.3) For this reason, the observed core shifts comprise the sum of both core shifts. Therefore, we decomposed the observed core shift into a westward shift for NGC 4261 and a northward shift for J1222+0413. However, the jet of NGC 4261 slightly bends from West to South, while the jet of J1222+0413 travels almost directly South. Indeed, the blob around -5 mas in the 8 GHz image of Figure 3.1 deviates southward from the East to the West, while the ridge lines at 2 GHz and 5 GHz incline toward the South beyond -5 mas. We measured the position of the ridge from the North to the South as -5 mas, corresponding to the position of the 1 GHz core in the 5 GHz image. From the deviation (-0.24 mas), we corrected the position of the core at 1 GHz.

Table 3.3: Core positions

ν (GHz) (1)	$r_{\rm AJ}$ (mas) (2)	$r_{\rm CJ}$ (mas) (3)
1.4	-4.92 ± 2.06	4.74 ± 2.05
2.3	-2.98 ± 0.79	2.73 ± 0.79
5.0	-1.18 ± 0.17	1.97 ± 0.17
8.4	-0.52 ± 0.08	1.60 ± 0.08
15	-0.21 ± 0.03	0.73 ± 0.33
22	-0.12 ± 0.02	0.29 ± 0.31
43	0 ± 0.02	0.17 ± 0.03

Columns are as follows: (1) frequency; (2) core position in approaching jet with respect to the core at 43 GHz; (3) core position in counter jet with respect to the core at 43 GHz in approaching jet.

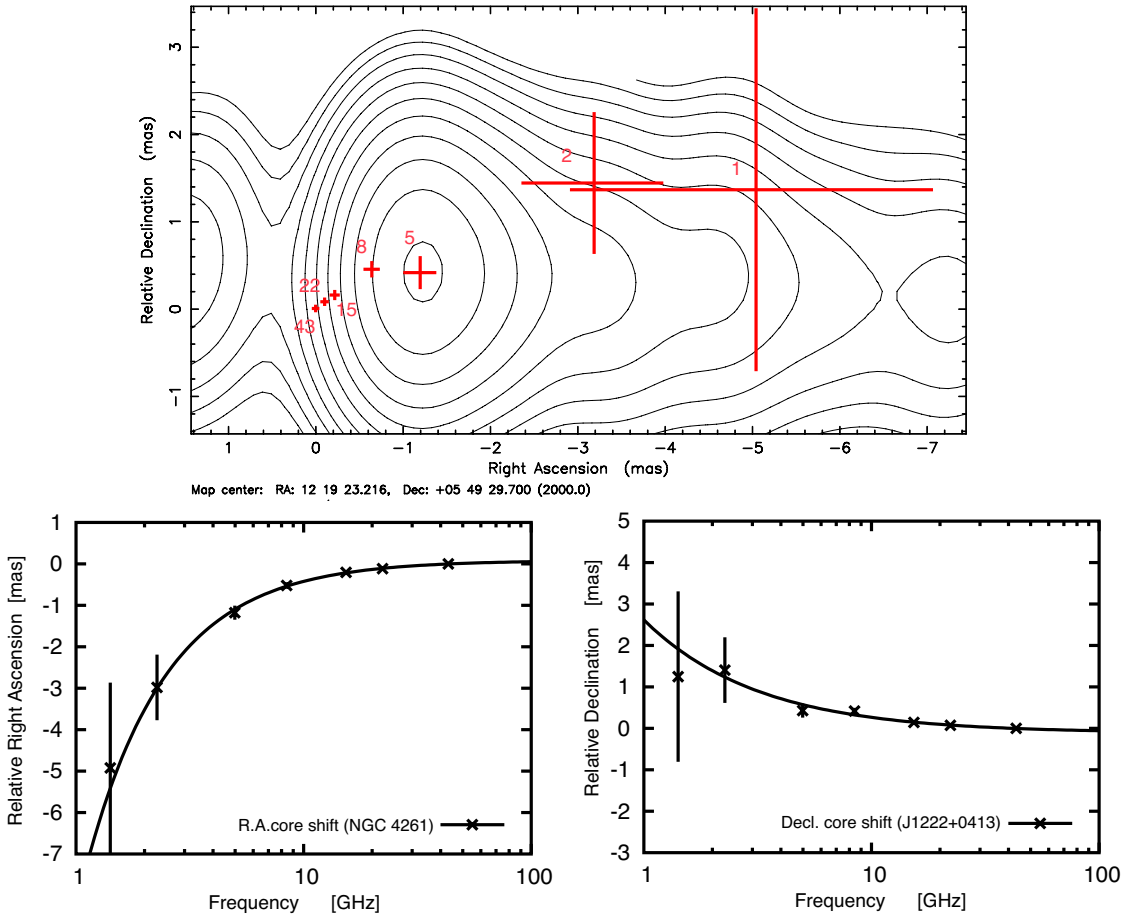

Figure 3.3: (Top) Red crosses denote the core positions at each frequency relative to the 43 GHz core on the same image. The thin contours denote the 5 GHz self-calibrated image. The core positions appear to drift northwest as the frequency is lowered. Given the jet directions of NGC 4261 and J1222+0413, NGC 4261 is responsible for the core shift in the right ascension direction, while J1222+0413 is responsible for the declination shift. (Bottom left) Shift in core position in right ascension as a function of frequency, attributable to NGC 4261. The solid line is the least-squares fitted function. (Bottom right) Frequency dependence of the declination shift in core position, caused by J1222+0413.

Figure 3.4 also reveals that the core position of NGC 4261 shifts at all other observational frequencies relative to the 43 GHz core. By least-squares fitting, the core position is found to shift as a power-law function of frequency; that is

$$r(\nu) = \Omega \cdot \nu^{-k} + b, \tag{3.1}$$

where Ω, k, and b are free-fitting parameters representing a scale factor, a power low index, and an asymptotic limit at infinite frequency, respectively. At the approaching jet side, these values are determined as $\Omega = -8.42 \pm 0.86$, $k = 1.22 \pm 0.06$, and $b = 0.082 \pm 0.016$, respectively, with residuals $\chi^2 = 0.16$ (see Table 3.4). The value of k is slightly, but significantly, larger than unity, as theoretically predicted for SSA under the equipartition condition and as frequently observed (Lobanov 1998; O'Sullivan & Gabuzda 2009; Sokolovsky et al. 2011; Hada et al. 2011). The asymptotic parameter b was determined within a tolerance of 32 μas ($\approx$ 120 $R_{\rm s}$) and separated by 82 μas ($\approx$ 310 $R_{\rm s}$) from the 43 GHz core position.

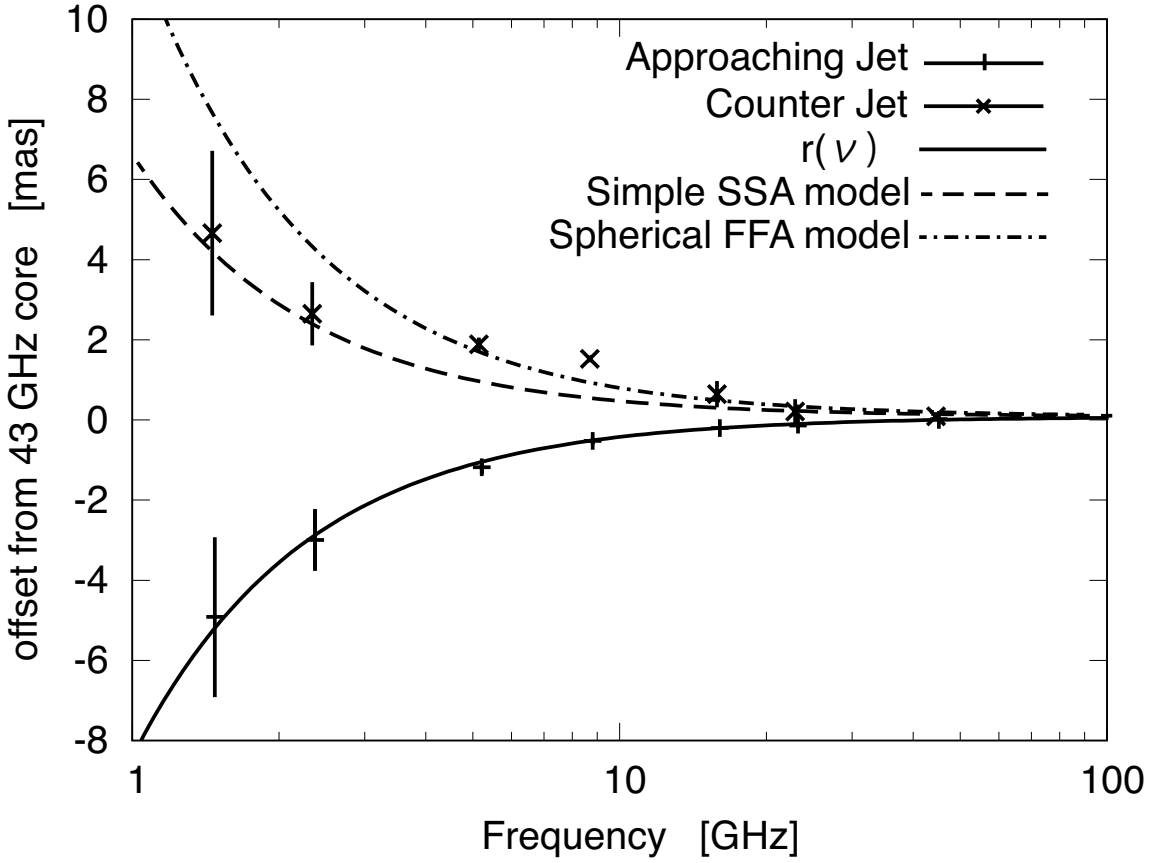

Figure 3.4: Core shift profile of the both side jet in NGC4261 Bars and crosses denote the core positions of the approaching and counter jets, respectively, in NGC4261. Solid lines are functions fitted by the least-square method. $r(\nu)$ is the curve shown in Figure 3.3. At the counter jet side, parameters were estimated by the SSA model (dashed line) and the spherical FFA plasma model (dot–dashed line). The values of k and b are equivalent to those of $r(\nu)$. Given the viewing angle, Ω at the counter jet side was estimated in both models from the results of the approaching jet side.

Table 3.4: Core shift fitting Parameters

	Ω	k	b	χ^2/n.d.f
	(1)	(2)	(3)	(4)
$r(\nu)$	-8.42 ± 0.86	-1.22 ± 0.06	0.082 ± 0.016	0.66/4

Columns are as follows: (1)–(3) parameters of the core shift fitting ; (4) reduced chi-square

We also measured and fitted the core shift at the counter jet side of NGC 4261. In this study, the core of the counter jet is defined as the closest east-side component to the core of the approaching jet, the region of maximum intensity yielded by `modelfit`. As shown in Figure 3.4, the distance between the cores in the approaching and counter jets reduces as the frequency

increases. However, when the shifting core of the counter jet was fitted to a three-parameter model, the errors in the parameters were unacceptably large. Thus, we applied two alternative model fitting procedures imposing further assumptions, which will be discussed in Section 4.2.

3.3 Spectral Index Maps

Spectral index (α, $S \propto \nu^{\alpha}$) maps were generated from final CLEANed images between two adjacent frequencies using the AIPS task `COMB`. To ensure proper construction of spectral index maps, the images between the adjacent frequencies must spatially align, and their angular resolutions must match. The map coordinates at each frequency were aligned using the core shift relative to the 43 GHz core in right ascension and the jet axis of NGC 4261 in declination. The images at adjacent frequencies were convolved by rendering both beams equivalent to the beam at the lower frequency. The intensity below 3σ was clipped out before calculating the spectral index.

All of the spectral index maps exhibit common features, in particular, the spectral index peaks in the regions between the cores of the approaching and counter jets. As the jet extends further from the core, the spectrum becomes steeper. Figure 3.5 displays the spectral index maps of the 1–2 GHz and 5–8 GHz frequency pairs. Some regions in the spectral index map, where $\alpha > 2.5$, cannot be explained by SSA alone. This result is consistent with other observations in which the circumnuclear structure favored FFA over SSA (Jones et al. 2001). The spectral index gradients are clearly parallel to the jet axis for all frequency pairs. The restored beams in each map are too large to decompose the absorption structures across the jet.

Figure 3.6 shows slice profiles of the spectral index map along the jet axis (from the East to the West). I estimated the error components in the spectral index. From the generated spectral index maps, I displaced the positional errors in the positive and negative directions when overlaying the images. Thus, I defined positional accuracy errors as envelopes from two slice profiles. I also used the spectral error map, simultaneously produced during `COMB` processing, and assumed a conservative flux calibration error of 5% at $\nu \leq 15$ GHz and 10% at $\nu \geq 22$ GHz. The total error represented by the envelope is the square root of the summed squares of both error components.

At $\nu \leq$15 GHz, a region of $\alpha > 2.5$ appears in the slice profiles, suggesting an FFA mechanism, although the error is too high for a conclusive assessment. Another feature is that the curve at $\nu \geq 5$ GHz peaks at the counter jet side. Moreover, the peaks are located at the same positions, regardless of the error-induced displacement of the core position. At $\nu \leq 2$ GHz, the peaks are located around the origin.

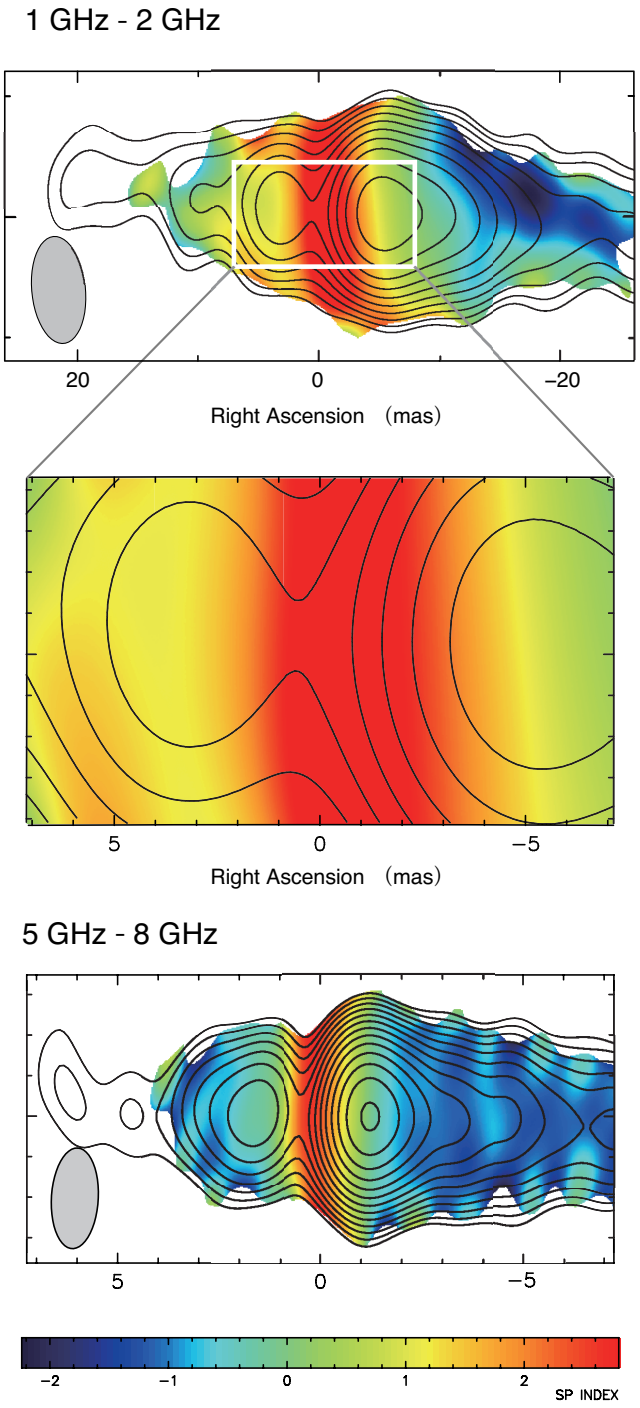

Figure 3.5: Spectral index maps between adjacent observation frequencies 1 GHz and 2 GHz (top) and 5 GHz and 8 GHz (bottom) synthesized after restoring the images with respect to the lower-frequency beam. In the map of the lower-frequency pair, the region covering ± 10 mas shows an inverted spectral index, indicating that absorption occurs over this region. The spectral index α is maximized at 3.5. In the map of the higher-frequency pair, the region of $\alpha > 2.5$ is located at the east side of the jet (at 0.4 mas), and the spectral index maximum is also positioned on the counter jet.

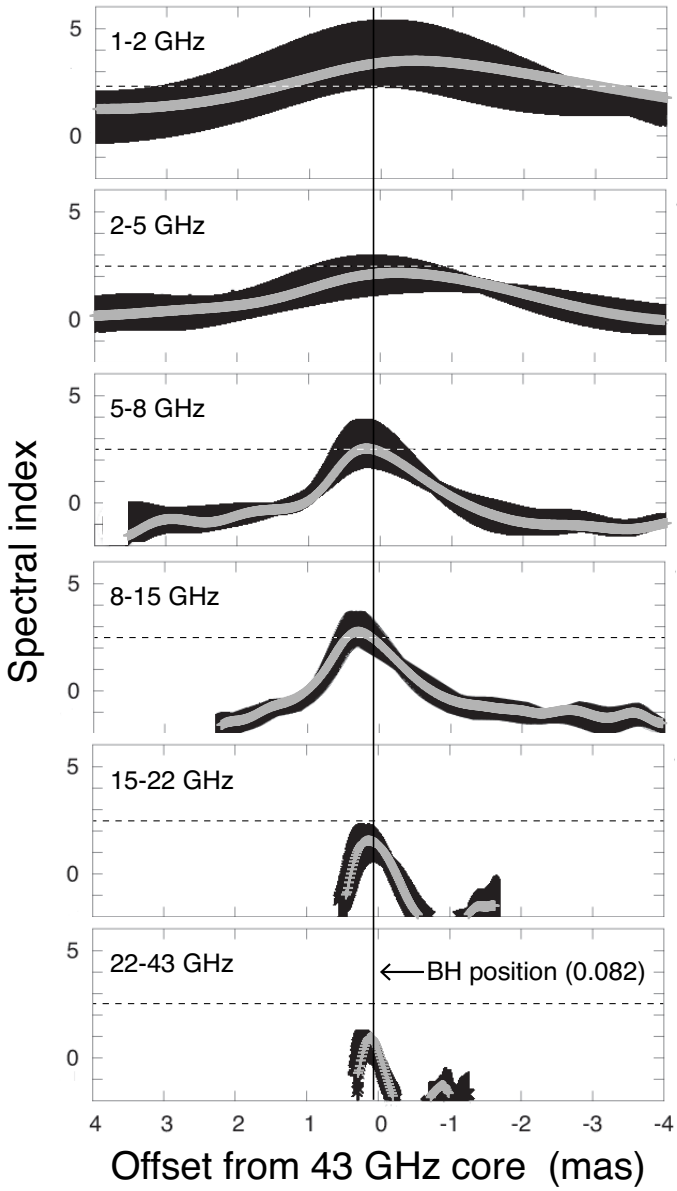

Figure 3.6: Profiles of spectral index maps along the jet axis at each pair of adjacent frequencies, centering on the core at 43 GHz. We estimated the errors in the spectral index, comprising the accuracy of the core position, flux calibration, and RMS of the image (see Section 3.3)

Gray narrow lines represents median values.

3.4 Jet Width

Figure 3.7–3.9 show the self-calibrated images using the multiple circular Gaussian model to fit VLBA visibility data. Red circle and a contour of each image denote Gaussian components and 3σ, respectively, where σ is RMS noise of the image. The determined parameters (the position, the FWHM of the Gaussian and the flux density) of each component are provided in Table 3.5–3.6. All images with uniform weight, alined relative to the 43 GHz core position were described successfully because the reduced χ square represents almost unity at all frequency.

Comparing the position of components at different frequencies, I identified the components at the same position. While the components at the outside region of the jet can be identified easily, it is difficult to distinguish those of the inner region near the core due to absorption effect. The component corresponding to the core should be cautiously treated. Figure 3.8 shows that the core component at 8 GHz is described by two Gaussian models. On the other hand, the same region at 5 GHz may be wedged into a single model as the photosphere ($\tau = 1$). It indicates that If the multiple components to radial directions is fitted by a single circular model, the jet width may be estimated excessively. Therefore, I did not use the core components for fitting the jet width profile. The circular Gaussian models in the pc scale approaching jet at all frequency are summarized in Figure 3.10 . The error bar in horizontal axis denotes the size of the model fitting component. At each frequency, the innermost components represent the core components and the core shifts are found clearly.

The VLA image at 1.4 GHz using the 17 circular Gaussian models is shown in Figure 3.11. The model fitting parameters at each components are listed in Table 3.7.

Table 3.5: Fitting parameters of the pc-scale jet (1–5 GHz)

ν	No.	Class	$r_{\rm RA}$	W	F	id
(GHz)			(mas)	(mas)	mJy	
(1)	(2)	(3)	(4)	(5)	(6)	(7)
1.4	1	CJ	18.3	6.7	5.6	C6
	2	CJ	9.4	2.7	5.8	C5
	3	CC	3.0	1.8	13.6	C3
	4	AC	-4.9	3.0	55.5	J6
	5	AJ	-9.9	2.9	28.9	J7
	6	AJ	-15.3	5.1	14.6	J8
	7	AJ	-24.6	6.6	10.2	J9
	8	AJ	-40.2	14.2	4.6	J10
2.3	1	CJ	9.8	5.2	6.5	C5
	2	CJ	5.7	1.2	7.7	C4
	3	CC	2.1	1.1	19.3	C3
	4	AC	-3.0	2.3	97.6	J5/J6a
	5	AJ	-6.2	2.4	33.3	J6
	6	AJ	-9.8	3.4	23.9	J7
	7	AJ	-15.5	4.7	8.5	J8
	8	AJ	-23.6	7.0	7.5	J9
5.0	1	CJ	5.0	3.1	10.2	C4
	2	CC	1.8	1.4	29.8	C3
	3	AC	-1.2	0.8	138.7	J3
	4	AJ	-2.5	1.0	46.6	J5a
	5	AJ	-4.4	1.6	41.3	J5b/J6a
	6	AJ	-7.0	1.9	22.3	J6b
	7	AJ	-9.8	2.6	13.5	J7
	8	AJ	-15.5	3.5	4.8	J8

Columns are as follows: (1) Frequency; (2) Number; (3) Classfication, where AJ, AC, CC, and CJ represent approaching jet, core at approaching jet, core at counter jet, and counter jet, respectively; (4) Positions in R.A. relative to 43 GHz core; (5) Components radius (FWHM); (6) Flux density; (7) Component ID to compare with those at different frequency

Table 3.6: Fitting parameters of the pc-scale jet (8.4–43 GHz)

ν (GHz)	No.	Class	$r_{\rm RA}$ (mas)	W (mas)	F mJy	id
(1)	(2)	(3)	(4)	(5)	(6)	(7)
8.4	1	CJ	2.9	1.4	7.1	C3b
	2	CC	1.4	1.2	21.7	C3a
	3	AC	-0.52	0.46	100.1	J3
	4	AJ	-1.1	0.58	73.1	J4
	5	AJ	-2.0	1.0	34.3	J5a
	6	AJ	-4.0	1.8	30.8	J5b/J6a
	7	AJ	-7.1	2.5	19.1	J6b
15	1	CJ	1.6	0.55	8.7	C3
	2	CC	0.63	0.68	9.3	C2
	3	AC	-0.21	0.27	135.2	J1
	4	AJ	-0.61	0.29	55.8	J2
	5	AJ	-1.1	0.43	41.9	J4a
	6	AJ	-1.9	0.82	21.9	J5a
	7	AJ	-3.9	1.4	13.6	J5b/J6a
	8	AJ	-6.5	1.6	8.2	J6b
22	1	CJ	1.5	0.24	3.0	C3
	2	CC	0.27	$\leq$0.01	7.2	C1
	3	AC	-0.12	0.15	139.0	J1
	4	AJ	-0.45	0.23	34.0	J2
	5	AJ	-1.0	0.5	25.5	J4a
	6	AJ	-1.5	0.37	4.9	J4b
43	1	CC	0.17	$\leq$0.01	6.1	C1
	2	AC	0	0.02	69.2	J1a
	3	AJ	-0.17	$\leq$0.01	9.5	J1b
	4	AJ	-1.0	0.54	4.3	J3

Columns are as follows: (1) Frequency; (2) Number; (3) Classfication, where AJ, AC, CC, and CJ represent approaching jet, core at approaching jet, core at counter jet, and counter jet, respectively; (4) Positions in R.A. relative to 43 GHz core; (5) Components radius (FWHM); (6) Flux density; (7) Component ID to compare with those at different frequency

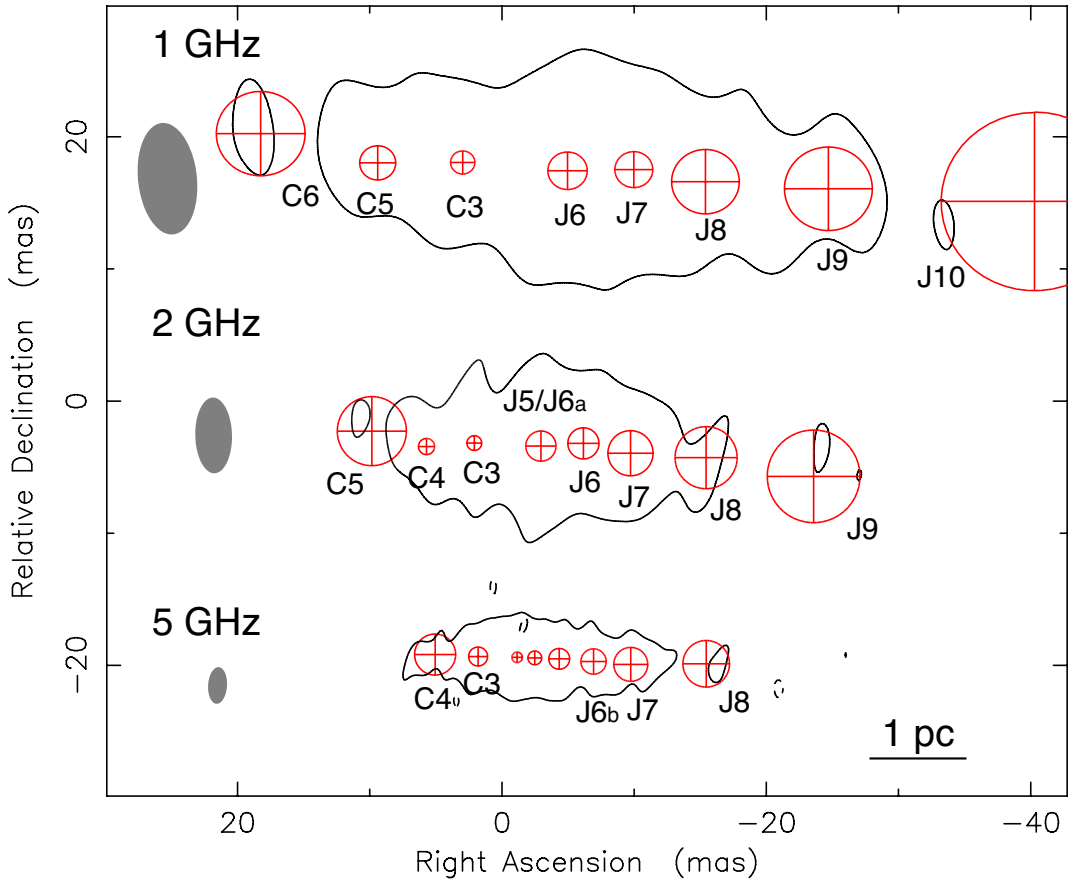

Figure 3.7: Images at three frequencies described by multiple circular Gaussian components using `modelfit` in Difmap. These images are aligned relative to 43 GHz core by taking account for core shifts. Red circles and contours at each map denotes Gaussian components and 3σ. 1.4 GHz ; the image is described by eight Gaussian components with reduced $\chi^2 = 0.96$. 2.3 GHz; the image is described by eight Gaussian components with reduced $\chi^2 = 1.13$. 5.0 GHz; the image is described by eight Gaussian components with reduced $\chi^2 = 1.08$.

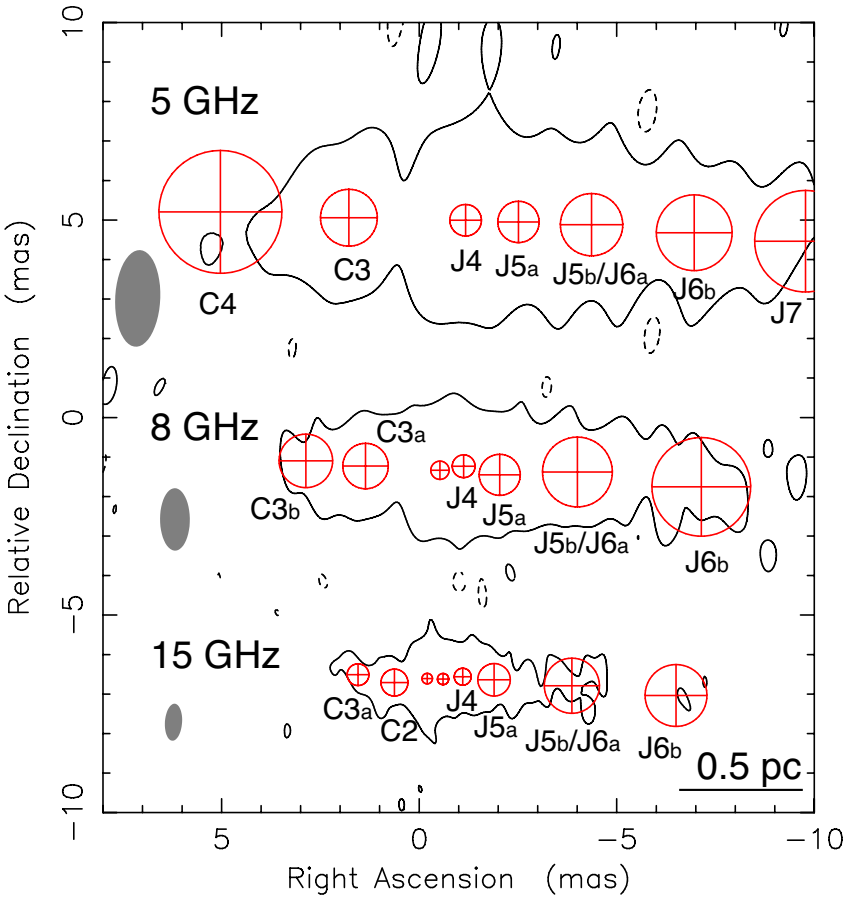

Figure 3.8: Images at three frequencies described by multiple circular Gaussian components using `modelfit` in Difmap. These images are aligned relative to 43 GHz core by taking account for core shifts. Red circles and contours at each map denotes Gaussian components and 3σ level of image noise level, respectively. 5.0 GHz ; the image is described by eight Gaussian components with reduced $\chi^2 = 1.08$. 8.4 GHz; the image is described by seven Gaussian components with reduced $\chi^2 = 1.07$. 15 GHz; the image is described by eight Gaussian components with reduced $\chi^2 = 1.04$.

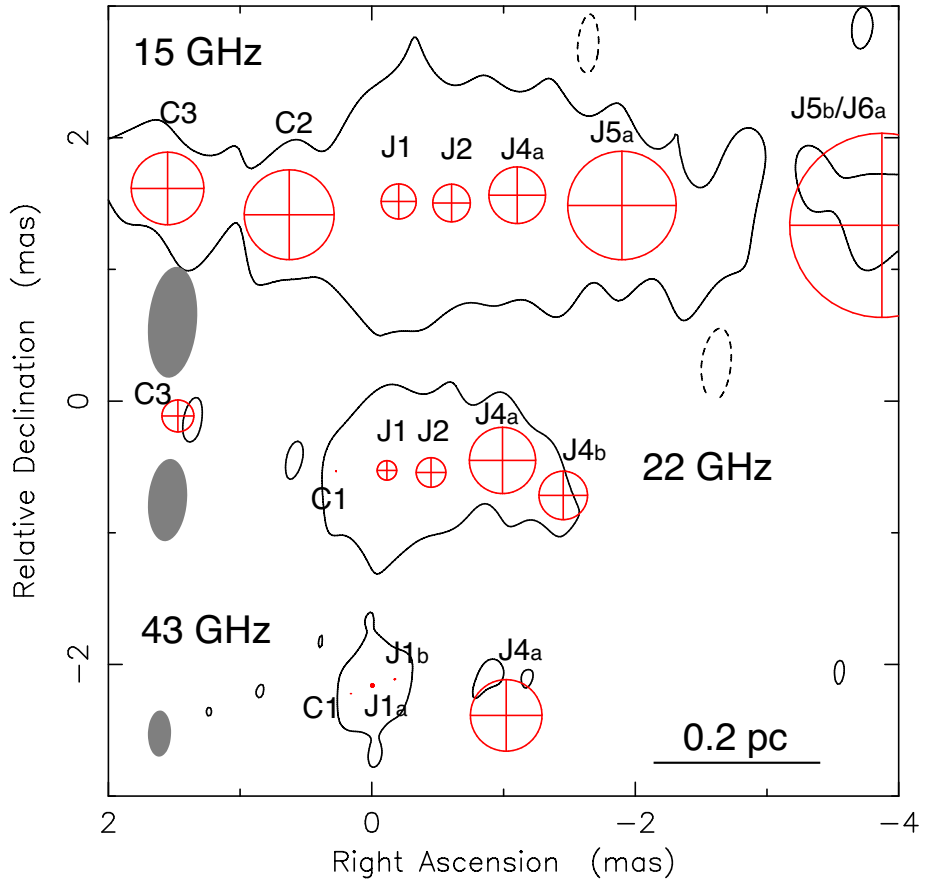

Figure 3.9: Images at three frequencies described by multiple circular Gaussian components using `modelfit` in Difmap. These images are aligned relative to 43 GHz core by taking account for core shifts. Red circles and contours at each map denotes Gaussian components and 3σ. 15 GHz ; the image is described by eight Gaussian components with reduced $\chi^2 = 1.04$. 22 GHz; the image is described by six Gaussian components with reduced $\chi^2 = 1.02$. 43 GHz; the image is described by four Gaussian components with reduced $\chi^2 = 1.00$.

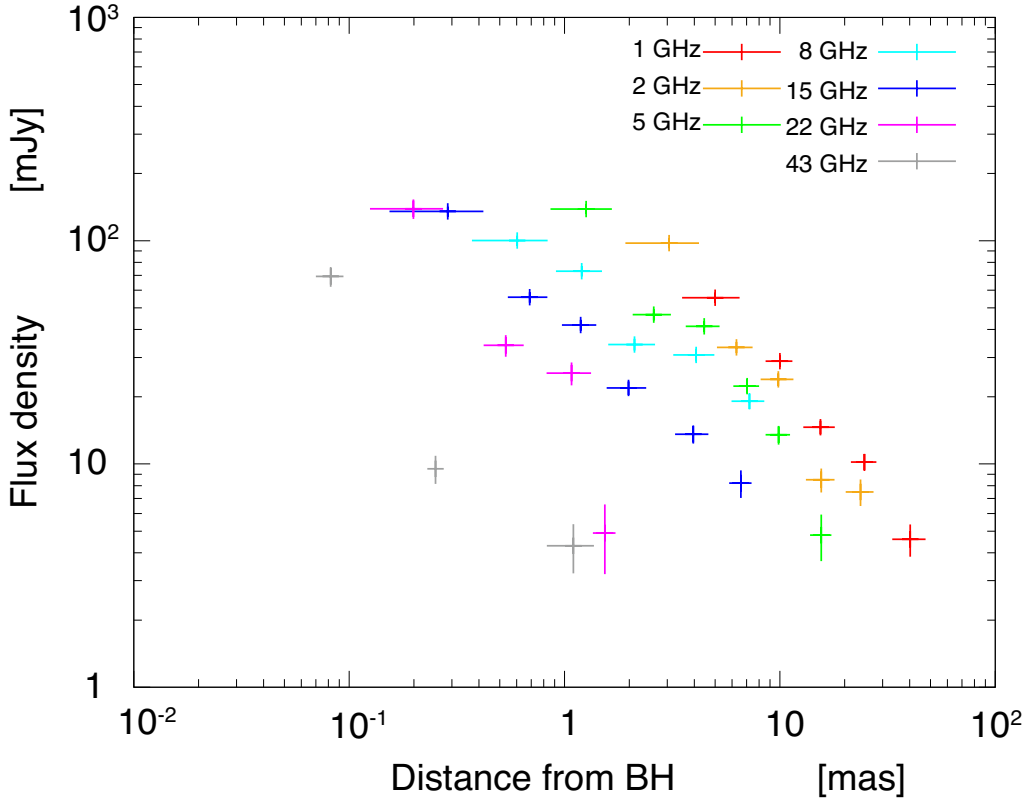

Figure 3.10: The comparison between the distance from the 43 GHz core and the flux. of the `modelfit` components. The error bars in distance represent the size of the components.

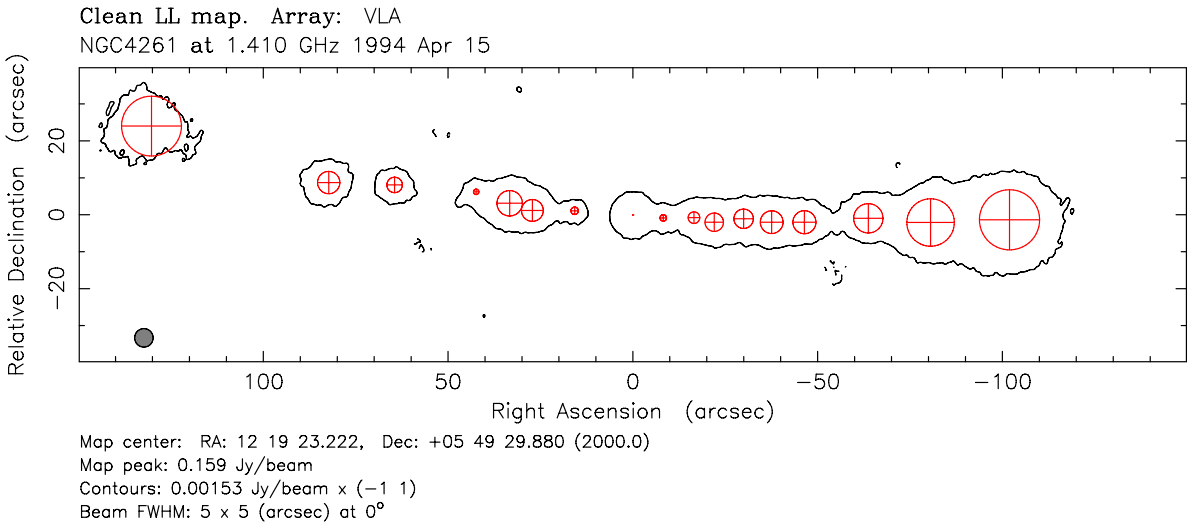

Figure 3.11: Self-calibrated images of NGC 4261 at 1 GHz using VLA using `modelfit` in Difmap. I fitted visibility data for some 2-dimension circular components.

Table 3.7: Fitting parameters of the kpc-scale jet

ν (GHz)	No.	Class	$r_{\rm RA}$ (as)	W (mas)	F mJy
(1)	(2)	(3)	(4)	(5)	(6)
1.4	1	CJ	4.96	16.2	21.60
	2	CJ	1.75	6.04	11.61
	3	CJ	0.55	4.19	6.81
	4	CJ	-0.93	1.47	4.18
	5	CJ	-1.53	6.88	37.92
	6	CJ	-1.95	5.90	16.97
	7	CJ	-2.71	2.01	4.51
	8	AC	-3.77	0.02	160.5
	9	AJ	-4.32	1.75	9.75
	10	AJ	-4.88	3.13	19.95
	11	AJ	-5.24	4.98	38.21
	12	AJ	-5.78	5.26	19.01
	13	AJ	-6.29	6.16	29.72
	14	AJ	-6.88	6.24	19.60
	15	AJ	-8.04	7.94	24.21
	16	AJ	-9.17	12.9	67.76
	17	AJ	-10.60	16.3	102.9

Columns are as follows: (1) Frequency; (2) Number; (3) Classfication, where AJ, AC, CC, and CJ represent approaching jet, core at approaching jet, core at counter jet, and counter jet, respectively; (4) Positions in R.A. relative to 43 GHz core; (5) Components radius (FWHM); (6) Flux density

3.5 Profile of the Jet Width

Next, I examine the development of the jet width along the jet direction. By least-squares fitting, the jet width profile is found to developed as a power-law function of the distance from the black hole; that is

$$W = W_0 x^a \tag{3.2}$$

where W_0 and a are free-fitting parameters representing the scaling factor and a power law index, respectively and x is the de-projected distance in R_s unit assuming $\theta = 63°$. I fitted VLBA data with Equation 3.2 and obtained the values, $W_0 = 0.96 \pm 0.25$ and $a = 0.90 \pm 0.03$. When fitting VLA data, I estimated the values, $W_0 = 2.91 \pm 2.92$ and 0.84 ± 0.05. The significant difference was not found between the index values in spite of the different scale. Therefore, I fitted the jet width at all range using single streamline. At the approaching jet side, these value are determined as $W_0 = 0.89 \pm 0.09$ and $a = 0.91 \pm 0.01$, respectively. The fitted profile of the jet width is shown Figure 3.12.

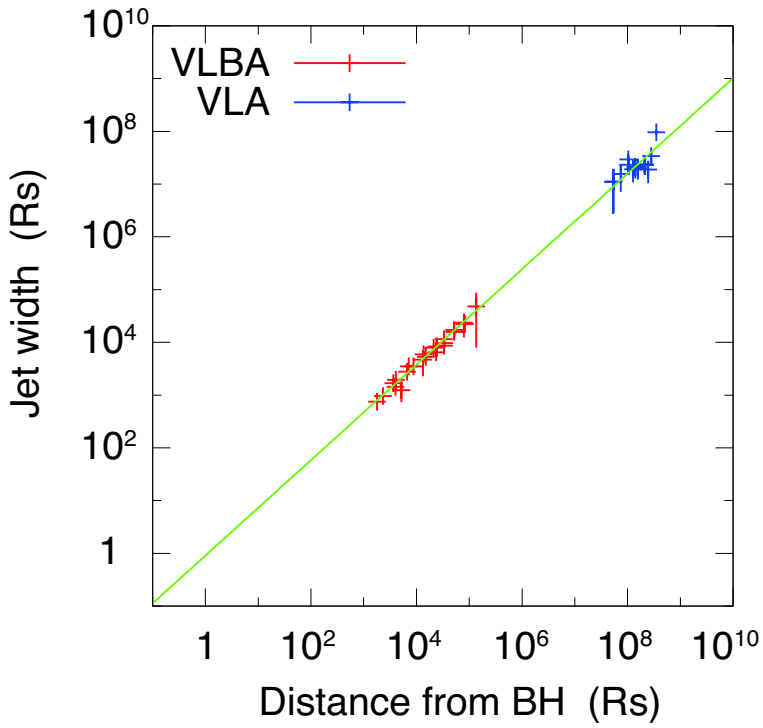

Figure 3.12: Red and blue represent VLBA data and VLA data, respectively. The green solid line is determined by fitting all data.

Chapter 4

Discussion

4.1 Position of the Black Hole

4.1.1 Position of the black hole in NGC 4261

First, we consider the relationships between the black hole positions and limiting core positions. Hada et al. (2011) showed that the central engine in M87 is located 23 $R_{\rm s}$ distant from the observed core at 43 GHz in their analyses of core shift measurements. This study assumed that the asymptotic line, representing the origin of a jet, spatially coincides with the black hole. However, the core location in the BL Lac object, indicated as the standing shock point (Marscher et al. 2008), is actually 10^4–10^6 $R_{\rm s}$ from the black hole, as determined from γ-ray monitoring observations (Albert et al. 2007). On the other hand, a core shift was discovered downstream of the BL Lac jet. Core shift measurements of BL Lac and other blazer sources reveal that the base of the jet is located 10^4 $R_{\rm s}$ from the 43 GHz core position (O'Sullivan & Gabuzda 2009). Recently, core shift data have accumulated at an accelerated pace for blazers (Sokolovsky et al. 2011; Pushkarev et al. 2012). However, the above-cited examples highlight the difficulty of proving assumptions from one-sided jets.

To overcome these limitations, we located the black hole in NGC 4261 by focusing on the counter jet. As shown in Figure 4.1, the core (most upstream component) at the counter jet side resides at 0.17 ± 0.03 mas ($\approx 640 \pm 110$ $R_{\rm s}$) from the approaching-jet core at 43 GHz.

The black hole must be situated at least 750 $R_{\rm s}$ distant from this core to ensure its location between the cores of both jets. Moreover, because the origin of the counter jet coincides with that of the approaching jet (as discussed later), the assumption that the origin of a jet spatially coincides with the black hole within the error tolerance is reasonable for NGC 4261.

4.1.2 Position of the Core at 43 GHz

The black hole of NGC 4261 is located at 82 ± 16 μas, corresponding to 310 ± 60 $R_{\rm s}$ from the 43 GHz core. The core/black-hole separation differs by orders of magnitude among NGC 4261, M87, and BL Lac, being larger and smaller in M87 and BL Lac, respectively, than in NGC 4261. The distance between the core position and black hole is correlated with the strength of SSA,

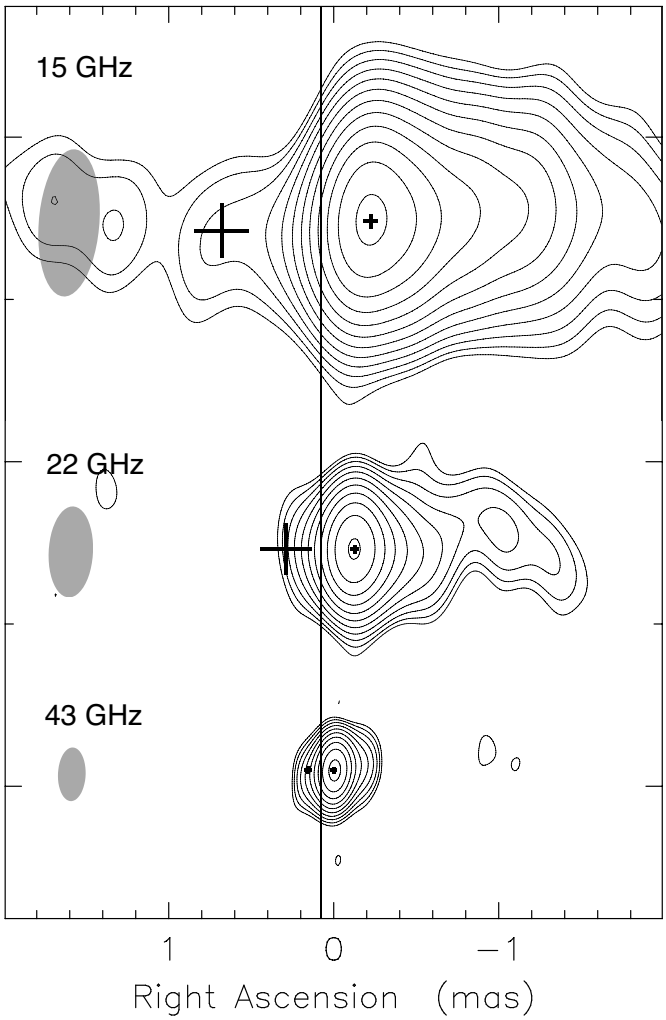

Figure 4.1: Enlarged image of Figure 3.1 at $\nu \geq 15$ GHz within $\pm$ 2 mas. The cross marks denote the positions at innermost cores at each jet side and the bars represents error size. The line at R.A. $= 0.082 \pm 0.016$ mas represents the determined position of the black hole.

and depends on jet characteristics such as luminosity, velocity, structure and/or the geometric relationship to our line of sight. According to Lobanov (1998), if a jet is continuous, uniform, stationary, and travels with constant velocity, and under equipartition condition, the core shift from the jet origin is given by

$$\Delta r_{\rm mas} \approx \frac{C_{\rm r}(1+z)}{D_L \gamma^2 \phi_0 \nu_1} \left[\frac{L_{\rm syn} \sin\theta}{\beta(1-\beta\cos\theta)\Theta} \right]^{2/3}, \tag{4.1}$$

where $C_{\rm r} = 4.56 \times 10^{-12}$, and $\gamma \equiv 1/\sqrt{1-\beta^2}$, $\beta \equiv v/c$, ϕ_0, and θ denote the Lorentz factor, the intrinsic jet velocity, jet opening angle, and viewing angle, respectively. $D_{\rm L}$ and $L_{\rm syn}$ are the luminosity distance to the source (parsec) and synchrotron luminosity (erg s^{-1}). In this case, Θ depends on the jet structure, whether conical or parabolic, and does not usually exceed $\ln 3$ for parsec-scale jets. The frequency ν is given in Hz. In this study, the separation between the

black hole and core position is determined at 43 GHz. Using Equation (4.1), we now compare the core/black-hole distance in NGC 4261 to those in M87 and BL Lac. In place of $L_{\rm syn}$, we use the intrinsic luminosity at millimeter wavelengths $L_{\rm m}$. In order to remove beaming effect from the observed luminosity $L_m^{\dagger}$, we calculate the beaming factor, δ using the viewing angle and intrinsic velocity at each source, where $\delta \equiv D^{3-\alpha}$ and $D = \gamma^{-1}/(1-\beta\cos\theta)$.

Using the parameter values $\theta = 63°$, $\beta = 0.46$ for NGC 4261 (Piner et al. 2001 and $L_{\rm m}^{\dagger} = 3.9\times10^{40}$ erg s^{-1} (Geldzahler & Witzel 1981), we estimated $\delta = 1.5$ and $L_{\rm m} = 2.4\times10^{40}$ erg s^{-1}, assuming $\alpha = -0.7$. The parameters of NGC 4261, M87, and BL Lac are provided in Table 4.1.

Assuming that the jet opening angle is nearly constant, thus, the ratio of the core/black-hole distance to that of NGC 4261 in $R_{\rm s}$ unit is given by

$$\Delta r_{\rm ratio} \approx 1.42 \left(\frac{(1-\beta^2)^{3/2}\sin\theta}{\beta(1-\beta\cos\theta)}\right)^{2/3} \left(\frac{M_{\rm BH}}{10^8 M_\odot}\right)^{-1} \left(\frac{L_{\rm m}}{10^{40}{\rm erg/s}}\right)^{2/3}. \quad (4.2)$$

For M87 case, the viewing angle of the jet is estimated to be 15°–25° (Acciari et al. 2009). From this viewing angle and the apparent jet velocity $\beta_{\rm app} = 0.25$ in the inner region (Ly et al. 2007), the estimated intrinsic velocity is $\beta \geqq 0.4$. Assuming $\beta = 0.4$, $\theta = 25°$ and $L_{\rm m}^{\dagger} = 5.2\times10^{40}$ erg s^{-1} (Davies et al. 2009), we obtain $L_{\rm m} \approx 1.4\times10^{40}$ erg s^{-1}. Adopting a black hole mass of $6\times10^9 M_\odot$ (Gebhardt & Thomas 2009), we obtained $\Delta r_{\rm ratio} = 0.04$. On the other hand, based on the core shift measurements, the 43 GHz-core/black-hole distance in M87 ($23R_{\rm s}$) to those in NGC 4261 ($310R_{\rm s}$) indicates $\Delta r_{\rm ratio} = 0.07$. The difference between the two results is only less than two times. The discrepancy may originate in uncertainties of the black hole mass or the intrinsic luminosity. Another possibility is an opening angle. From Equation (4.1), the separation is inversely proportional to the opening angle. If the opening angle of M87 is widely larger (e.g, (Junor et al. 1999)) than that of NGC 4261, it can explain the difference of the separation between them.

Table 4.1: parameters for comparison

Object name	Δr_{43}	$M_{\rm BH}$	β	θ	δ	$L_m^{\dagger}$	L_m
	$[R_{\rm s}]$	$[10^8 M_\odot]$				$[10^{40}$ ergs$^{-1}]$	$[10^{40}$ erg s$^{-1}]$
(1)	(2)	(3)	(4)	(5)	(6)	(7)	(8)
NGC 4261	310 ± 60	4.9	0.46	63°	1.5	3.9	2.5
M 87	23 ± 6	60	0.4	15°–25°	3.8	5.2	1.4
BL Lac	10^4-10^6	1.7	0.99	6°–10°	3.6×10^3	3.6×10^3	1.0

Columns are as follows: (1) object name; (2) distance of the core at 43 GHz from the black hole; (3) black hole mass; (4) jet velocity on the light speed; (5) jet inclination (6) beaming factor ($D^{3-\alpha}$, where $D \equiv 1/\gamma(1-\beta\cos\theta)$) (7) observed luminosity at millimeter wave range, (8) estimated intrinsic luminosity

By contrast, the core shift in BL Lac substantially differs from that of NGC 4261. The $\Delta r_{\rm ratio}$ of BL Lac is 30–3000. The estimated jet velocity and inclination are $\beta = 0.99$ and $\theta = 6°$–$10°$,

respectively (Jorstad et al. 2005). Such conditions should enhance the relativistic beaming effect, and indicate $\delta = 3.6 \times 10^3$. Since the observed luminosity was reported to be 3.6×10^{43} erg s^{-1}, we estimate an intrinsic luminosity as $L_{\rm m} \approx 1 \times 10^{40}$ erg s^{-1}. The mass of the black hole associated with BL Lac is estimated to be $1.7 \times 10^8 M_\odot$ (Woo & Urry 2002 Substituting these value into Equation (4.2), we obtain $\Delta r_{\rm ratio} \approx 0.08$, showing a large discrepancy from the result from core shift observations. To explain the large discrepancy, a much larger intrinsic luminosity of $L_{\rm m} \geq 7 \times 10^{43}$ erg s^{-1} or a much smaller opening angle $\phi_0 \leq 0.08$ deg.

However, such a wide difference in intrinsic luminosity between NGC 4261 and BL Lac is quite unlikely if both FR-I radio galaxies and BL Lac are regarded as a common ANG population intrinsically, low luminosity AGNs (LLAGNs) (Urry et al. 1991). More likely, the appearance of FR-I radio galaxies and BL Lac differ because of the beaming effect imposed by jet inclination. The jet of M87 has a limb-brightened structure, which is probably associated with a fast spinal flow surrounded by a slow layer (sheath) (Ghisellini et al. 2005). If the jet axis inclines significantly from the line of sight, for as in M87 and NGC 4261 as FR-Is, sheath emission dominates, because spinal emission is de-boosted by the relativistic effect. On the other hand, if the jet is viewed from nearly pole-on, for such as BL Lac, spine emission from a small opening angle dominates. This phenomenon can explain the varying distance between the black hole and the 43 GHz core between FR-I radio galaxies and BL Lac.

4.2 What Cause the Core Shift

The physical causes of the core shift are considered as SSA and/or FFA. Here, we establish the model that best explains the core shift of NGC 4261, focusing on the results of fitting parameters in Equation (3.1). Although the core shift could not be closely fitted at the counter jet side, the parameters at this side can be estimated from those of the approaching side in each model.

4.2.1 SSA in Jets

First, we assume a pure SSA model. The physical conditions in the jet reflect the index of the core shift profile in Equation (3.1). In this model, k_s (representing k for SSA case) is given by

$$k_{\rm s} = \frac{5-2\alpha}{(3-2\alpha)m+2n-2}, \tag{4.3}$$

where α, m and n denote the spectral indexes, the profiles of the magnetic field B (where $B \propto r^{-m}$), and the electron density N (where $N \propto r^{-n}$), respectively (Blandford &Königl 1979). Assuming $m = 1$ and $n = 2$ as the profile indexes, corresponding to the stabilization of jet energy in equipartition, $k_{\rm s}$ invariably becomes unity regardless of the spectral index value. However, the fitting parameter at the approaching jet side is $k_{\rm s} = 1.22 \pm 0.06$, slightly, but significantly, higher than unity. This result, which differs from previous studies for other sources ($k_{\rm s} \approx 1$; i.e., M87, BL Lac, and 3C345), indicates that m and n in Equation (4.3) can take different values in NGC 4261.

We next predict the core shift profile at the counter jet side assuming the SSA model. If the jets are intrinsically symmetric, $k_{\rm s}$ and b of the counter and approaching jets side should be identical. However, comparing Equations (3.1) and (4.1), we find that Ω depends on geometrical and intrinsic parameters of a jet. The parameter Ω differs between the approaching and counter jets only through the inclination, θ. Therefore, Ω of the counter and approaching sides, denoted $\Omega_{\rm CJ}$ and $\Omega_{\rm AJ}$, respectively, must satisfy $\Omega_{\rm AJ} > \Omega_{\rm CJ}$. In other words, the position of the core at the same frequency is farther from the black hole in the approaching jet than in the counter jet. The parameter $\Omega_{\rm CJ}$ should be connected with $\Omega_{\rm AJ}$ and the viewing angle of NGC 4261. The curve predicted by the pure SSA model (dashed line in Figure 3.4) can explain the core position at both low frequency ($\leq$ 2 GHz) and high frequency ($\geq$ 22 GHz). On the other hand, the observed positions of the core at 5, 8, and 15 GHz are significantly larger than those predicted by this model, implying that the SSA model alone lacks sufficient absorption to explain the core shift.

4.2.2 Spherical FFA Plasma

Another alternative is the FFA model. The spectral index maps indicate that FFA plasma exists at least in regions near the black hole. For simplicity, and from the parameters of the core shift measurement, we assume a spherical FFA plasma. In this case, k depends on the structure of the spherical FFA plasma. When the FFA opacity $\tau_{\rm f}$ becomes unity, k_f (representing k in Equation (3.1) for FFA model) is given by

$$k_{\rm f} = \frac{2.1}{2s - \frac{3}{2}t - 1}, \tag{4.4}$$

where s and t represent the profiles of the electron density $n_{\rm e}$ and temperature T_e ($n_e \propto r^{-s}$, $T_e \propto r^{-t}$) in the FFA absorber, respectively. Although the parameters of the absorber are not directly determined, they can be predicted from the opacity profile; the denominator in the right side of Equation 4.4 represents the index value of the opacity profile. We obtain the radial profile of FFA opacity at the approaching jet side by fitting to a power-low function; $\tau_{\rm f} \propto r^{-1.6}$. Substituting this value into Equation (4.4), we obtain $k_{\rm f} = 1.3$. It is consistent with the result of the core shift measurements ($k_{\rm f} = 1.22 \pm 0.06$) if the core shift at approaching jet side is caused by spherical FFA. Theoretical speculations have indicated that $k_{\rm f}$ exceeds unity (Lobanov 1998; Kadler et al. 2004. Thus, the core shift at approaching jet side can be sufficiently interpreted by the spherical FFA model.

However, the spherical FFA is inconsistent with the radial profile of FFA opacity on the counter jet side. The parameter $k_{\rm f}$ should be identical in both the approaching and counter sides if the FFA absorber is symmetric. In the FFA model, Ω then reflects the path length of the absorber; that is, the geometrical structure of the absorber (for details, see Appendix C) . If the absorber covers the counter jet side with disk-like or spherical structures, Ω must satisfy $\Omega_{\rm AJ} < \Omega_{\rm CJ}$, because the path length of the counter jet is longer than that of the approaching jet. The curve predicted by the spherical FFA plasma model (dot–dashed line in Figure 3.4) meets most of core positions at ≥ 5 GHz on the counter jet side. However, the core shifts at 1 and 2 GHz are inconsistent because their shifts are significantly smaller than those predicted by this model.

Therefore, neither of these simple models can explain the core shifts at both sides.

4.2.3 SSA in Jet + FFA by the Disk

A possible solution is to combine the SSA core shift with an additional external absorber, which compensates for the inadequate core shift. Indeed, my results show that the pure SSA model fitted fairly well on both approaching and counter sides at all frequency, except for the counter-jet components at 5, 8, 15 GHz, within the error tolerance. When the core shifts are fitted without the cores at these frequencies, the best-fit values of $k = 1.15 \pm 0.06$ and $b = 0.081 \pm 0.017$ (representing the index and the asymptotic limit in this condition) approximate those of the approaching side, as expected from SSA theory (Table 3.4). This suggests the presence of an absorber in a limited region. Thus, it appears that the cores at 5, 8, and 15 GHz are additionally affected by FFA. A possible radial profile of FFA opacity $\tau_{\rm f}$ at the 2–22 GHz core of the counter jet is shown in Figure 4.2; on the 5–15 GHz core, $\tau_{\rm f}$ is given by the spectral shape fitting (for details, see Appendix C), and $\tau_{\rm f}$ at other frequencies should be $\tau_{\rm f} < 1$.

The FFA regions indicated in the spectral index maps at these frequencies match those of previous studies (Jones et al. 2001). Thus, the geometrically thin disk predicted in previous studies is a candidate to explain the core shift of both sides.

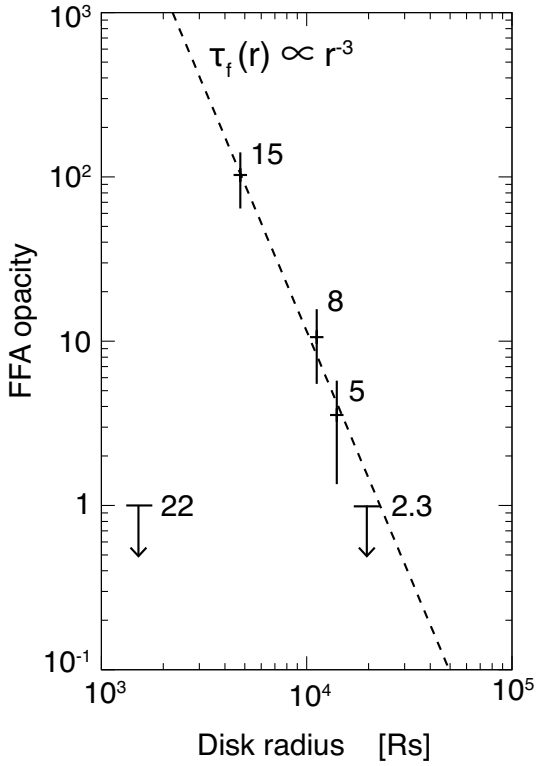

Figure 4.2: FFA opacity profile at the counter jet side (for details see Appendix). The low frequency (2 GHz) and the high frequency (22 GHz) denote upper limit. The dashed line denotes the radial profile of $\tau_{\rm f}$ as a power-low function of r by least-square fitting with 5–15 GHz data.

4.3 Disk structure of NGC 4261

I consider the structure of a disk to explain the core shift and the profile of $\tau_{\rm f}$ at the counter jet side.

4.3.1 Disk Model

Figure 4.3 shows the geometric relationships between the jet and disk, assuming $\theta = 63^\circ$ and the rotation axis of the disk is aligned with the axis of pc-scale jet. As discussed in the combined model, if the disk plasma cause the core shift at 5–15 GHz, the density and temperature of the disk require the radial gradient ($n_{\rm e} = n_0 x^{-s}$, $T_{\rm e} = T_0 x^{-t}$, where x is the radius of the disk in $R_{\rm s}$ unit, $r = xR_{\rm s}$). In addition, the thickness of the disk and the path length through the disk to observers are also described as $H = H_0 x^{-h}$ and $L = H \sec\theta$. By substituting $n_{\rm e}$, $T_{\rm e}$ and L into Equation (A.3), I obtain $\tau_{\rm f}$ by the disk (hereafter $\tau_{\rm disk}$); that is

$$\tau_{\rm disk} = 0.46 n_0^2 T_0^{-3/2} H_0 \sec\theta x^{-(2s-3t/2-h)}. \tag{4.5}$$

In the Figure 4.2 the least-squares fitting at at 5–15 GHz data reveals the profile of disk

opacity to the power-law function of the disk radius; that is $\tau_{\rm f} \propto r^{-3}$, then I obtain

$$2s - \frac{3}{2}t - h = 3. \tag{4.6}$$

4.3.2 Small core shift in $\nu < 2$ GHz, and $\nu > 22$ GHz

To explain the small opacity at low frequency (≤ 2 GHz), the low density, the short path length or high temperature are required because the FFA effects depend on frequency ($\tau \propto \nu^{-2.1}$). In these requirements, the condition of the path length and the temperature are physically unrealistic because the low frequency core positions correspond to the outer radii of the disk. Therefore, it is realistic that the density is sufficiently small and/or the temperature of the plasma is too low to be ionized.

I consider the condition that the temperature at the radius corresponding to the 5 GHz core position and at the 2 GHz are higher and lower than 10^4 K, respectively. Assuming that $t = 3/4$ predicted by standard disk model at the outer region (Shakura & Sunyaev 1973) and 10^4 K at 5 GHz, I obtain

$$T_{\rm e} = 1 \times 10^7 x^{-3/4} ({\rm K}). \tag{4.7}$$

In addition, if $h = 0$ (wherever the path length is constant) and $H_0 = 0.01$ pc, for simplicity, I obtain $s = 2$ from Equation (4.6). It is almost close to $s = 15/8$ predicted by standard disk model. Inserting these value and $\tau_{\rm disk}$ to Equation (4.5), I obtain

$$n_{\rm e} = 8 \times 10^{12} x^{-2} \ \ ({\rm cm}^{-3}). \tag{4.8}$$

The density and temperature profile in this condition is shown in Figure 4.3.

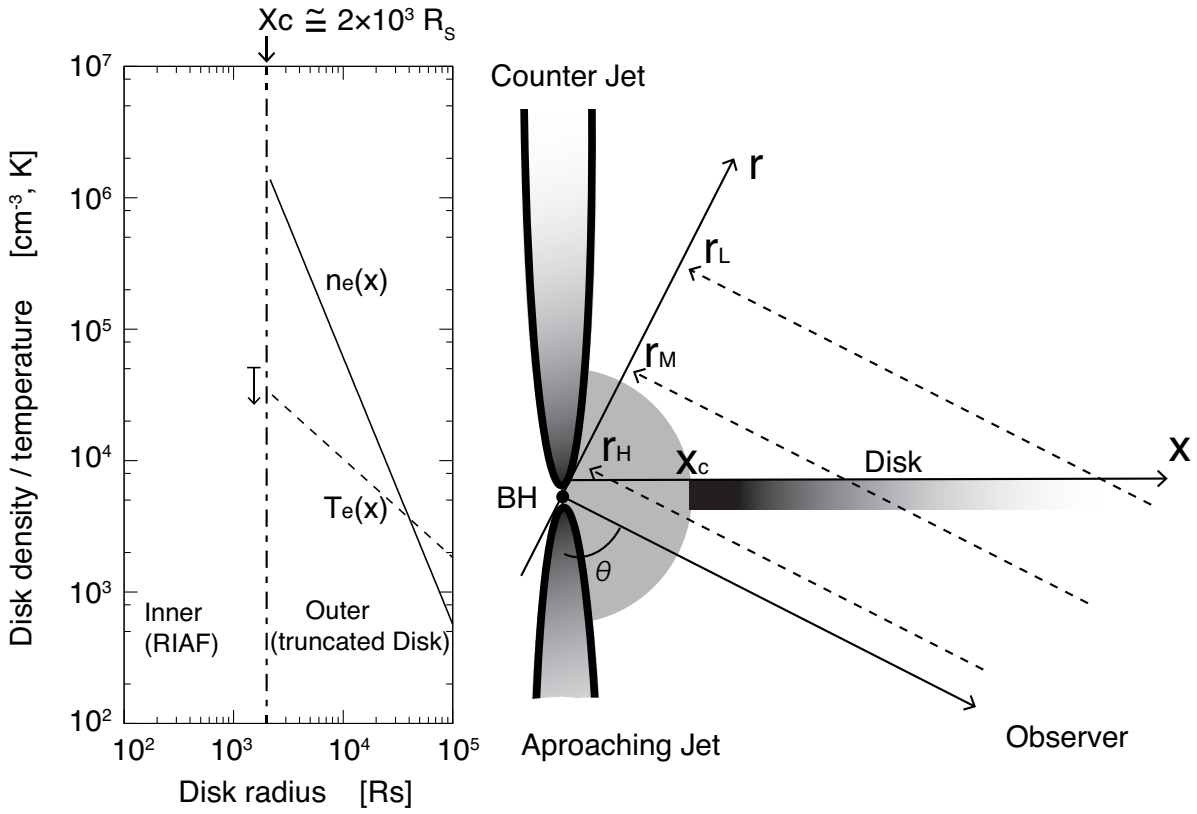

Figure 4.3: (Left) Profiles of the disk density ($n_{\rm e}$) and temperature ($T_{\rm e}$) assuming $t = 0.75$, 10^4 K at the area covering the 5 GHz core in the case of $h = 0$ and $H_0 = 0.01$ pc. An arrow denotes the upper limit of $n_{\rm e}$ at 22 GHz, calculating from $T_{\rm e}$ and $\tau_{\rm disk} < 1$. (Right) Schematic illustration of our model that simultaneously explains the observed core shifts in the jets at both sides. The parameters $r_{\rm H}$, $r_{\rm M}$ and $r_{\rm L}$ denotes the observational core position at the high frequency ($\leq$ 22 GHz), the medium frequency (5–15 GHz) and the low frequency ($\geq$ 2.3 GHz) range, respectively. At $r_{\rm H}$ and $r_{\rm L}$, the counter jet is not absorbed sufficiently because of the obscuration only by optically thin disk at inner region, and the low electron density due to the the low temperature at outer disk. On the other hand, at $r_{\rm M}$ the counter jet is strongly absorbed by the trucked disk. x_c represent the transition radius of the structure.

I note that the assumptions of h, and H_0 may be unsupported and thus other values are acceptable. Substituting $h = -9/8$(predicted by standard disk model) into Equation(4.6) and $H_0 = 2 \times 10^{-6}$ pc (corresponding to $L = 0.01$ pc at the 5 GHz core), I obtain $s = 2.6$ and $n_0 = 2 \times 10^{15}$ cm^{-3}. Although the index parameter, s increase the gap to the value predicted by the model, $n_{\rm e}$ at $x = 10^3$–10^5 is almost the same within a few times factor comparing to the case of $h = 0$. In the case of H_0, $n_{\rm e} \propto H_0^{-0.5}$ is obtained from Equation (4.5), indicating the thinner disk geometrically requires the higher density (i.e., $n_0 = 8 \times 10^{13}$ cm^{-3} at $H_0 = 10^{-4}$ pc). However, if the disk thickness was much larger (i.e., $H_0 > 1$ pc), the disk would obscure the approaching jet as well as the counter jet. Thus, $H_0 = 0.01$ pc provide a reasonable upper limit, indicating the lower limit of $n_{\rm e}$.

On the other hand, calculating the $\tau_{\rm disk}$ at 22 GHz ($x = 1.5 \times 10^3$), this density profile cannot explain the small opacity at high frequency ($\geq$ 22 GHz). At the inner region (22 GHz), the plasma temperature is sufficiently high to reduce FFA effect; at outer region (2 GHz), the temperature is too low to ionize gas ($T < 10^4$ K). However, this is impractical because the disk temperature at 3 $R_{\rm s}$ should be too high (10^{14} K). The explanation of the FFA opacity at the 22 GHz core requires either the lower density than that of outside or the rapidly-increasing temperature, indicating that the disk structure changes dramatically at a characteristic radius. The RIAF model is suitable for describing this situation such as the low density and high temperature. In fact, X-ray observations suggested that low X-ray luminosity of NGC 4261 and flux and spectral variations of the nuclear X-ray emission be caused by the accretion disk with low accretion rate and low radiative efficiency such as RIAF(Gliozzi et al. 2003).

Therefore, I propose the accretion flow of NGC 4261 has a two-component structure; one is an inner, hot, optically thin, RIAF and the other is an outer, truncated, cool, optically thick accretion disk. This structure is considered to be not special for NGC 4261 but common for LLAGNs based on broad spectral energy distribution (SED) and X-ray spectra studies(Nemmen et al. 2006; Nandra et al. 2007).

4.3.3 Comparison of the Theoretical Model of the Transition Radius

According Liu et al. (1999), the transition radius, x_c is given by

$$x_c = 18.3 m_b^{0.17/1.17} \dot{m}_b^{-1/1.17} \tag{4.9}$$

where m_b and $\dot{m}_b$ denote the black hole mass in units of solar masses, $M_{\rm BH} = m_b M_\odot$ and mass accretion rates in Eddington units, $\dot{M} = \dot{m}_b \dot{M}_{\rm Edd}$, $\dot{M}_{\rm Edd} = L_{\rm Edd}/0.1c^2 = 1.39 \times 10^{18} m_b$ g s^{-1}. Inserting $x_c = 2 \times 10^3$ ($x_{22} = 1.9 \times 10^3$) and $m_b = 4.9 \times 10^8$ to Equation (4.9), I obtain $\dot{m}_b = 0.12$, indicating this is slightly higher accretion rate compared to that of the typical LLAGNs ($\dot{m}_b = 10^{-2}$–10^{-3}). Recently, the equation of the transition radius is modified by the disk evaporation model taking account the effects of viscosity and magnetic field in accretion flow (Qiao et al. 2013). In this case, $x_c = 2 \times 10^3$ is easily acceptable for m $10^{-3} < \dot{m}_b < 10^{-2}$ in Figure 4.4.

Consequently, this combined model of RIAF and truncated disk is a possible solution to

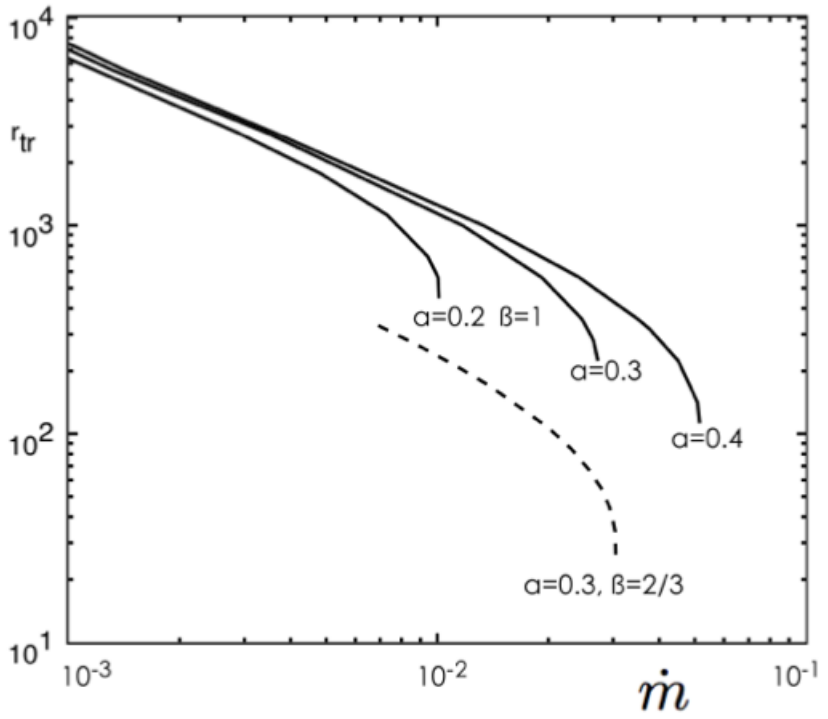

Figure 4.4: Variation of the truncation radius with respect to the mass accretion rate for specific values of the viscosity parameter α_t and magnetic parameter β_t as predicted by the disk evaporation model(Taam et al., 2012). Solid lines are for the case without magnetic effects and the dashed line show the effect of magnetic field.

explain the core shift of NGC 4261 at both side simultaneously. Figure 4.3 show this schematic illustration.

4.4 Jet Structure

My result of NGC 4261 is the second example of measuring the jet width with reference to the position of the black hole position accurately. Here, I approach the jet structure by comparing to the case of M87, which is examined most closely for the first case.

A clear difference of the jet profile between two sources shows in the power-law index of Equation (3.2), which represents the shape of the jet . The value of M87 ($a = 0.58$) at the upstream ($r < 10^5 R_{\rm s}$) indicates the parabolic and collimated shape while that of NGC 4261 shows $a = 0.91$ corresponding to a conical shape.

This difference may be closely related to the acceleration of the jet. Although the jet of M87 at the inner region (10^3–10^4 $R_{\rm s}$, corresponding to 0.6–6 pc) is presumed to be modest velocity ($\geqq 0.4c$), the components at $\sim 10^5$ $R_{\rm s}$ ($\sim$ 60 pc) known as "HST-1", is estimated to reach into $\sim c$ based on superluminal motion with a range of $4 \sim 6$ c (Biretta et al. 1999; Giroletti et al. 2012). Moreover, HST-1 is also characterized by γ-rays emission (Harris et al. 2006. Therefore, the jet of M87 is interpreted as the acceleration and the collimation at the parabolic region and then, the γ rays emits due to the hydrodynamic recollimation shock. On the other hand, superluminal motion or γ rays in the jet of NGC 4261 are not found even though the modest velocity (0.46c) was measured at about $10^4 R_{\rm s}$ (Piner et al. 2001). This is consistent with the conical shape, indicating no or less acceleration.

In order to determined the mechanism of jet formation, higher resolution observations and polarized observations are required because the magnetic filed have an important part in the jet trigged by MHD. Compared to M87, the magnetic field of NGC 4261 near the core was estimated to be very weak (0.4%) by high sensitivity, VLBA observations (Kharb et al. 2005), indicating apparently the difference of the mechanism of jet formation. However, if rich plasma gases are located around the jet, it is difficult to distinguish the reasons of the weak magnetic filed due to Faraday depolarization or due to generating jet by another mechanism. The investigation of other sources are also required.

Chapter 5

Conclusion

5.1 What Are Revealed ?

I measured the origin of the jets at the radio galaxy NGC 4261 as the limit of the core position using a core shift profile. The origin is 82 ± 16 μas distant from the 43 GHz core position, corresponding to 310 ± 60 $R_{\rm s}$. I also measured the core shift at the counter jet side and confirmed that the core positions at both sides asymptotically converges to the same limit. Therefore, I conclude that the jet origin estimated by core shift measurements spatially coincides with the black hole.

The spectral index maps reveal the possible presence of FFA, $\alpha > 2.5$, at the counter jet side. The core shift profile of the counter jet is not solely attributable to synchrotron self-absorption and requires an additional absorbing component with a disk-like structure. Moreover, the opacity profile requires two-component such as a combined model of RIAF and truncated disk interpreted as the accretion flows of LLAGNs. I suggest a possible solution of the density and temperature profile in outer disk, $T_{\rm e} = 1 \times 10^7 x^{-3/4}$ K and $n_{\rm e} = 8 \times 10^{12} x^{-2}$ cm^{-3}, respectively, assuming $H_0 = 0.01$ pc .

I measured the jet width of NGC 4261 through the range from 10^3–10^9 $R_{\rm s}$. The jet shape is maintained with almost conical ($W \propto r^{0.91 \pm 0.03}$) indicating less acceleration. This profile is significantly different from that of another nearby radio galaxy, M 87, whose index indicate the collimation and acceleration by MHD jet.

Figure 5.1 summarize what my thesis revealed.

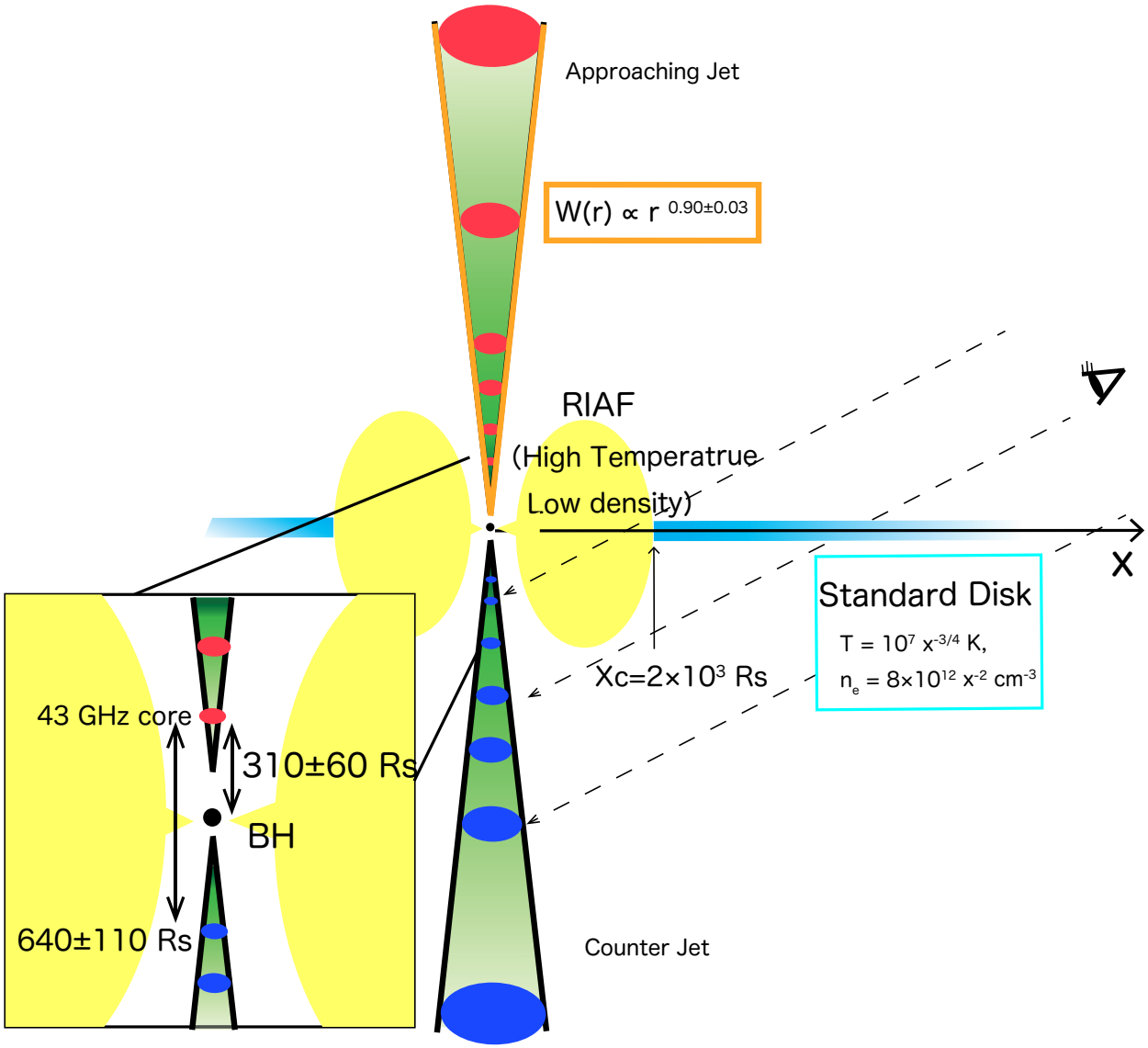

Figure 5.1: Schematic diagram summarizing our thesis. I estimate the position of the black hole (a black dot) by measuring the core positions at approaching jet (red ellipses) and counter jet (blue ellipses). I propose a solution of the disk structure explaining the results of spectral index map and opacity profiles. My model of the accretion disk consists of two components, RIAF (yellow ellipses) with high temperature and low density) at inner region, and standard disk (light blue squares) with temperature of $10^7 x^{-3/4}$ K and density of $8 \times 10^{12} x^{-2}$ cm^{-3}. The profile of the jet width propose that the jet is shaped like a conical jet, indicating not to be collimated and accelerated.

5.2 Future Prospects

This thesis reveals the position of the black hole and the structure of the accretion disk of NGC 4261, while the structure of the jet still remains as unsolved problems. For instance, I do not determine that the jet is generated from whether the black hole or the accretion disk. Furthermore, the generation mechanism of the jet is still not fully understood. Then, it is important to investigate the relationship between the jet structure and the accretion disk and compare the structures between the approaching jet and the counter jet.

In order to bring an end to these disputes. the observations with a higher spatial resolution and a higher sensitivity are required. For the high spatial resolution, the VLBI observations at higher frequency is an effective solution. Future sub-millimeter VLBI observation is one of the leading projects, expected to resolve the structure of the more inner jet base and to image a black hole event horizon. However, the characteristics of absorption present at low frequency. Then, the observation of the low-frequency with a long baseline such as a space VLBI project, will be also important. Furthermore, telescopes with high sensitivity can observe the structure accurately. Of course, Atacama Large Millimeter/submillimeter Array (ALMA) is one of the most significant project in radio band. Now, although the resolution is not enough to image a central engine, a extended ALMA project will contribute in the future. My study will play a rule of milestone to these future project.

Although NGC 4261 is the most successful case for investigating the structure of the central engine, the method in my study can be applied for other sources. I have already selected candidates and obtained other VLBA data. Increasing of observational examples enables to understand the structure of the central engine more generally.

Appendix A

Core Shift Theory

In this appendix, I introduce the theory of core shifts. Following Lobanov (1998), core shifts are mainly caused by two processes; one is synchrotron self-absorption in jets, the other is free–free absorption by plasma gases surrounding a central engine.

A.1 Core Shift due to Synchrotron Self-Absorption

A highly collimated jet can be formed by an ambient plasma with steep pressure and density gradients along the rotational axis of the accretion disk. The jet geometry can be approximated by a conical or paraboloidal expansion, with he transverse radius $W \propto r^a$ $(a \geq 1)$ for most of parse-scale jets. Assuming that the jet opening angle $\phi = \arctan(W/r)$ is constant for $a = 1$, the magnetic field and particle density decrease with r, and can be approximated as $B(r) \propto r^{-m}$ and $N(r) \propto r^{-n}$. The combination $m = 1$, $n = 2$ can be used to describe the observed X-ray and synchrotron emission from the most compact regions of VLBI jets (Köonigl 1981. Figure A.1 summarize the jet geometry of this situation.

At any given frequency, the VLBI core is observed at the location where the optical depth of synchrotron self-absorption is $\tau_{\rm s} = 1$. For $N(r)$ and $B(r)$, the corresponding $\tau_{\rm s}$ is (e.g. Rybicki & Lightman 1979):

$$\tau_{\rm s} = C N_1 \left(\frac{eB_1}{2\pi m_{\rm e}} \right)^{\epsilon} \frac{\delta^{\epsilon} \phi_o}{r^{(\epsilon m + n - 1)} \nu^{\epsilon + 1}}, \tag{A.1}$$

where N_1, B_1 are the electron density and the magnetic field at $r = 1$ pc. The observed jet opening angle $\phi_o = \phi \csc\theta$ is described in Blumenthal & Gould (1970) and $m_{\rm e}$ denotes the electron mass. The index ϵ and C are described as $\epsilon = 3/2 - \alpha$ and $C = 8.4 \times 10^{10}$, respectively. Substituting $\tau_{\rm s} = 1$ in Equation (A.1) and solving the equation for r, I obtained the distance from the central engine to the core:

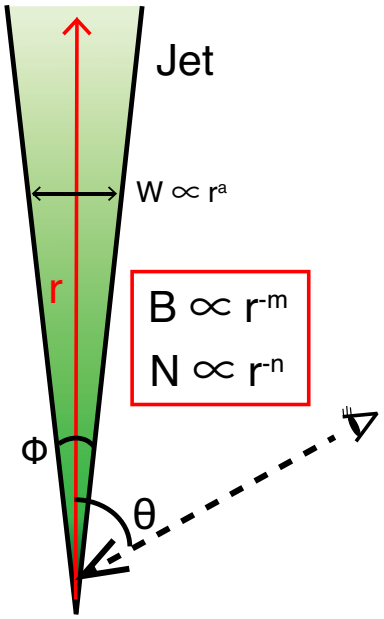

Figure A.1: Schematic jet geometry in SSA. The magnetic field and particle density decrease with r. I assume the conical jet, whose transverse radius represents $W \propto r^a$ for $a = 1$. The jet opening angle and the viewing angle denotes ϕ and θ.

$$
\begin{aligned}
r &= \left(CN_1 \left(\frac{e}{2\pi m_{\rm e}} \right)^{\epsilon} \phi_0 \delta^{\epsilon} \right)^{\frac{1}{\epsilon m+n-1}} B_1^{\frac{\epsilon}{\epsilon m+n-1}} \left(\frac{1}{\nu} \right)^{\frac{\epsilon+1}{\epsilon m+n-1}} \\
&= \left(\left(CN_1 \left(\frac{e}{2\pi m_{\rm e}} \right)^{\epsilon} \phi_0 \delta^{\epsilon} \right)^{\frac{1}{\epsilon+1}} B_1^{\frac{\epsilon}{\epsilon+1}} \frac{1}{\nu} \right)^{\frac{1}{k_r}} \\
&= \left(B_1^{k_b} F/\nu \right)^{1/k_r}
\end{aligned}
$$

Here,

$$
\begin{aligned}
F &= \left(CN_1 \left(\frac{e}{2\pi m_{\rm e}} \right)^{\epsilon} \phi_0 \delta^{\epsilon} \right)^{\frac{1}{\epsilon+1}} \\
k_b &= \frac{3-2\alpha}{5-2\alpha} \\
k_r &= \frac{(3-2\alpha)m + 2n - 2}{5-2\alpha}
\end{aligned}
$$

The choice of $m = 1, n = 2$ appear to be the most reasonable and the equipartition value of $k_r = 1$. In this case, the corresponding k_r does not depend on spectral index, and then, the core shift of SSA depends on $\propto \nu^{-1}$.

A.2 Core Shift due to Free–Free Absorption

Foreground free–free absorption in a hydrogen plasma is expected to affect the radio core emission propagating thorough a dense nuclear environment.

Similar to the SSA core shift, I can estimate the FFA-induced core shift using the radial profile of FFA opacity. The spectral shape S_ν of FFA is described as

$$S_\nu = S_0 \nu^{\alpha_0} \exp(-\tau_f \nu^{-2.1}), \tag{A.2}$$

where

$$\tau_{\rm f} \backsimeq 0.46 \left(\frac{n_{\rm e}}{1{\rm cm}^{-3}}\right)^2 \left(\frac{L}{1{\rm pc}}\right) \left(\frac{T_{\rm e}}{1{\rm K}}\right)^{-1.5}. \tag{A.3}$$

Here, S_0, α_0 and $\tau_{\rm f}$ are the unabsorbed flux density at 1 GHz, the intrinsic spectral index of synchrotron emission, and FFA opacity, respectively; $n_{\rm e}$, L and $T_{\rm e}$ are the electron density, path length, and temperature of the plasma, respectively. Assuming that the core position affected by FFA is emitting at the local maximum in the spectral shape, the partial derivative of (A.2) with respect to ν is maximized at $\alpha + 2.1\tau = 0$, where $\tau = \tau_{\rm f}\nu^{-2.1}$. Finally, I obtain

$$\tau_{\rm f} = \frac{-\alpha}{2.1}\nu^{2.1} \tag{A.4}$$

If the electron density and temperature of the FFA plasma follow a power-law function, i.e., $n_{\rm e} = n_0 r^{-s}$ and $T_{\rm e} = T_0 r^{-t}$, Equation (A.4) can be rewrite as

$$\begin{aligned} \tau_0 r^{-2s+3t/2+1} &= \frac{-\alpha}{2.1}\nu^{2.1} \\ r(\nu) &= \Omega_{\rm FFA}\nu^{-k_{\rm f}} \end{aligned} \tag{A.5}$$

where

$$k_{\rm f} = \frac{2.1}{2s - 3t/2 - 1}$$

and $\Omega_{\rm FFA}$ denotes a scaling factor. Unlike in the case of SSA, the analysis of the FFA core shift requires the assumption of the absorbed structure because $\Omega_{\rm FFA}$ and $k_{\rm f}$ depended highly on parameters of the structure (s,t,n_0,T_0 and L). I discuss two simple cases in Chapter 4 and Appendix C.

Appendix B

Details of Positional Error Estimation about Core Shift

In order to discuss the core shift, the careful treat of the error estimation is required. According to supplementary information in Hada et al. 2011, I estimated the error of the core shift. The component of the error in the core shift measurement consists of dispersive ionospheric residuals, non-dispersive tropospheric residuals, core identification process, geometrical parameters (earth orientation parameters, antenna positions and apriori source coordinates) and the quality of the phase-referencing images. In this appendix, I explain the details of the positional accuracy in phase-referencing observations.

Ionosphere

Dispersive ionospheric medium contribute to the propagation delays. When conducting phase-referencing analyses, I assumed that the radio waves from both a target and a calibrator will pass thorough the nearly the same part of the propagating medium. However, if the correction residual remains, a small separation of the positions between both sources cause uncertainty. Therefore, I should estimate this uncertainty.

First, I estimate the correction residual between phase-referencing analysis. This effect are usually corrected by AIPS task `TECOR` using Global ionospheric model based on GPS satellites. As the model have an accuracy of about $10 \sim 25$ % (Mannucci et al. 1999), I adapt the uncertainty of 25%. Assuming that the ionosphere spread like a parallel plate, the potential remaining errors $\delta\theta$ after the correction can be estimated through the equation (Lestrade et al. 1990).

$$\delta\theta \sim \frac{c\delta\tau_{0,\mathrm{ion}}}{B} \sec Z tan Z \delta Z, \tag{B.1}$$

where c, $\delta\tau_{0,\mathrm{ion}} = 40.3\delta I/\nu^2$ (Thompson et al. 2001), Z, δZ and B represent the speed of light residual ionospheric zenith delay (with residual total electron content δI in m^{-2} and frequency ν in Hz), zenith angle, source separation (radian), and baseline length (m). Global ionospheric model in this observation showed the value of $I \sim 3 \times 10^{17}$ m^{-2} at most over the sky of VLBA stations at a maximum although the observations coincide with the 2003 solar maximum.

Substituting $\delta I \sim 7.5 \times 10^{16}$ m^{-2}, $Z = 50°$, $\delta Z = 1.7°$ and $B = 8.6 \times 10^{6}$ m, the results at each frequency are summarized in Table 2.1.

Troposphere

The non-dispersive tropospheric medium cause propagation delays. Similarly to the ionospheric medium, an inaccurate tropospheric zenith delay in a correlator model contributes to uncertainty in the core shift. I adapt 1.0 cm as the error accuracy conservatively in my observations since the delay caused by the water vapor fluctuation on time scale of hour to day typically remains ranging from 0.1 $\sim$ 1.0 cm (Treuhaft & Lanyi 1987). Then, I replace $c\delta\tau_{0,ion}$ in Equation B.1 with $c\delta\tau_{0,ion} = 10^{-2}$ m. By substituting the same for the other conditions in the case of the ionosphere, I obtained the positional uncertainties of 13 μas at all frequency.

Beam width/ signal to noise

Inaccuracy of ionosphere and troposphere model also cause the effect of the image distortion which contributes to the positional random error in a phase-referenced image. According to Thompson et al. 1995, this positional accuracy is estimated as

$$\delta\theta \sim \theta_b \frac{1}{2\pi SNR} \tag{B.2}$$

where θ_b and SNR are the interferometric beam size and the signal-to-noise ratio of the phase-referenced image, respectively. Therefore, the positional accuracy can be improved if I obtain the phase-referenced image with sufficient SNR.

Core Identification

The method of core identification also contributes to the position uncertainties. If the source has a core-jet structure, the accuracy of the core position requires to discriminate between the core and the jet emission. I identified the core of NGC 4261 using `modelfit` in Difmap, which fits the calibrated visibility data with model components. I modeled the the core and the jet emission as multiple circular Gaussian components at all frequency. Figure B.1 shows an example of `modelfit` with visibility data and image at 15 GHz.

I evaluated the presumable uncertainties of the core positions by comparing these positions with alternative method independent of `modelfit` which effectively also extracts the position of the core from the mix of the core-jet emission. The structure of NGC 4261 was de-convolved by the CLEAN algorithm. I then convolved it with a circular Gaussian beam of full-width at half-maximum (FWHM) about a half of synthesized beam in the core-jet direction and obtained a super-resolution map of which I defined the core position as the brightness peak. The core position derived from this method is also shown in Figure B.2 as a black filled circle. I adopted the difference between the positions using two method at each frequency as the positional accuracy of the core identification.

This result of the estimation is provided in Table 2.1. The frequency dependence show different features between the approaching jet and counter jet. Although the error is usually

expected to be small with the small synthesize beam, it is depended on the structure of the core. Therefore, the behavior of the error most likely become complex because the structure change due to the observing frequency.

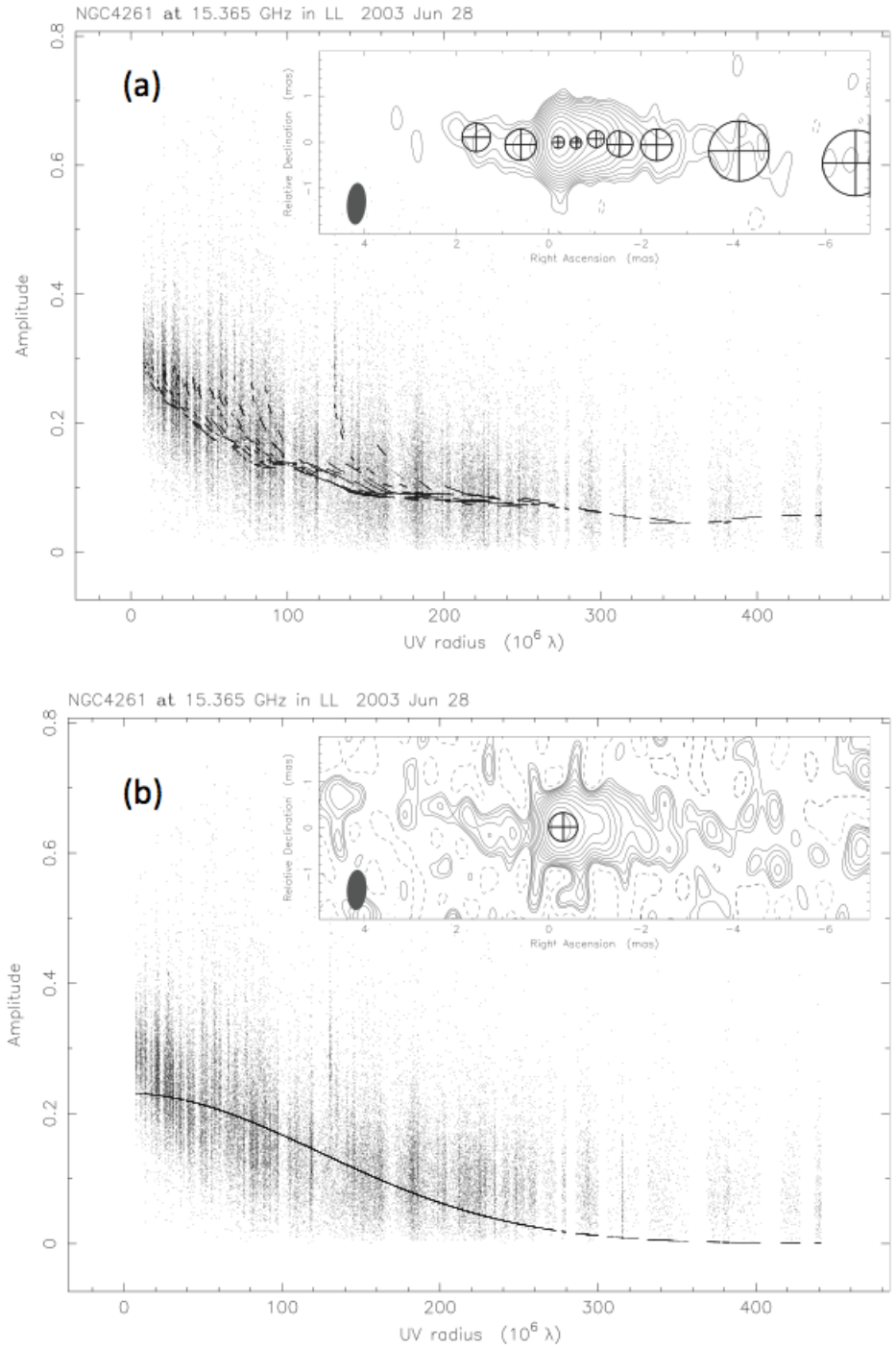

Figure B.1: Examples of visibility amplitude and best-fit model with Gaussian components using `modelfit`. Dots and thick lines represent the observed visibility amplitude at each *uv* distance and the best-fit model. (a): Case for multi Gaussian components, (b): Case for single Gaussian component. Increasing the model components can describe the visibility more accurately. Each map at right top made by each best-fit model.

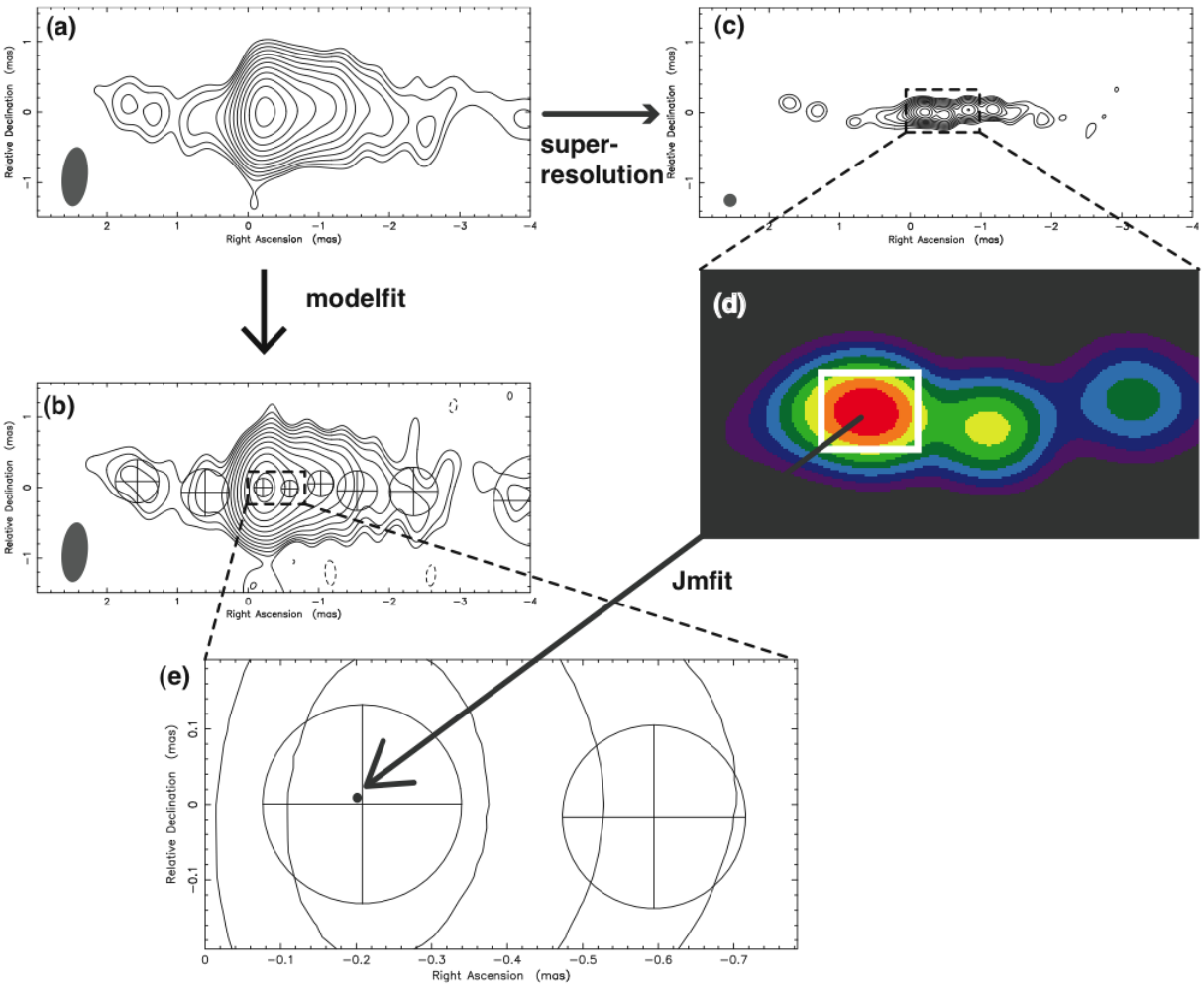

Figure B.2: Comparison between two method to evaluate accuracy of core identification. (a) Self-calibrated image at 15 GHz made by a CLEAN algorithm . (b) Image made by fitting visibility data with multi-circular Gaussian components (`modelfit`). (c) Super-resolution image with a circular Gaussian beam about a half of synthesized beam. (d) Enlarged image of (c). I measured the peak position by fitting the image in a white box with two-dimensional Gaussian model (`Jmfit`). (e) Enlarged image of (b). A black circle represents the position determined by `Jmfit`. The separation between two positions was measured to be 3 μas.

Appendix C

Spherical FFA plasma model

This appendix details the methods used to estimate the FFA opacity profile and FFA core shifts. FFA is an alternative core-shifting process to SSA. The spectral index maps at low frequencies, especially, the 1–2 GHz adjacent pair, indicate that the FFA region of $\alpha > 2.5$ extends across not only the counter jet and the core but also the approaching jet. This result implicates FFA as a potential cause of the core shift in the approaching jet.

C.1 Analysis of the FFA opacity profile

First, I estimated the distribution of FFA opacity along the jet axis (from the East to the West). I determined an intensity profile along the jet by integrating the flux density of clean components in defined regions, at intervals of 0.25 mas and 1 mas inside and outside of 2 mas from the putative BH, respectively. From the integrated flux densities, I then performed spectral fitting analysis in each area. The fitting function for spectral shape with Equation (A.2). Assuming that α_0 is fixed at some typical value ($\alpha_0 = -0.7$), S_0 and $\tau_{\rm f}$ were determined by least-squares fitting. Figure C.1 shows the determined distribution of FFA opacity $\tau_{\rm f}$. In addition, I determined the radial profile of FFA opacity at the approaching jet side by fitting to a power-law function;

$$\tau_{\rm f} = \tau_0 x^{-d}, \tag{C.1}$$

where, τ_0, d and x are free-fitting parameters. The fitted parameters are listed in Table C.1.

Table C.1: The result of the parameters about the opacity profile using least-square fitting

Side	τ_0	d
(1)	(2)	(3)
A-Jet	$(1.24 \pm 0.21) \times 10^7$	-1.65 ± 0.02
C-Jet	$(0.53 \pm 2.88) \times 10^7$	-1.66 ± 0.65

Col. 1: Jet side Col. 2: The FFA opacity at 1 $R_{\rm s}$. Col. 3: The index parameter.

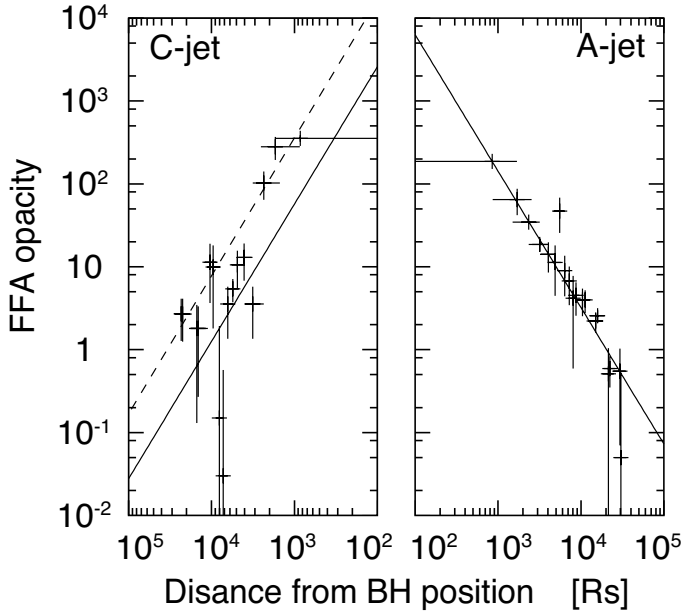

Figure C.1: FFA opacity profiles at the counter jet (left) and approaching jet (right) sides. Crosses denote the opacity in each area, and the solid lines denote the least-square fits to the function $\tau_{\rm f} = \tau_0 r^{-d}$. The dashed line at the counter jet side denotes the maximum error range of τ_0. The fitting parameters are given in Table C.1.

C.1.1 Core shift due to spherical FFA plasma

Substituting this τ into (C.1) and solving the equation for x, I obtained the core shift profile at the approaching jet side.

Assuming the structure of the FFA plasma, the core shift profile at the counter jet side can be derived from the information of the approaching side. In this study, I presumed a simple spherical plasma (see Figure C.2), which can obscure both the approaching jet and the counter jet.

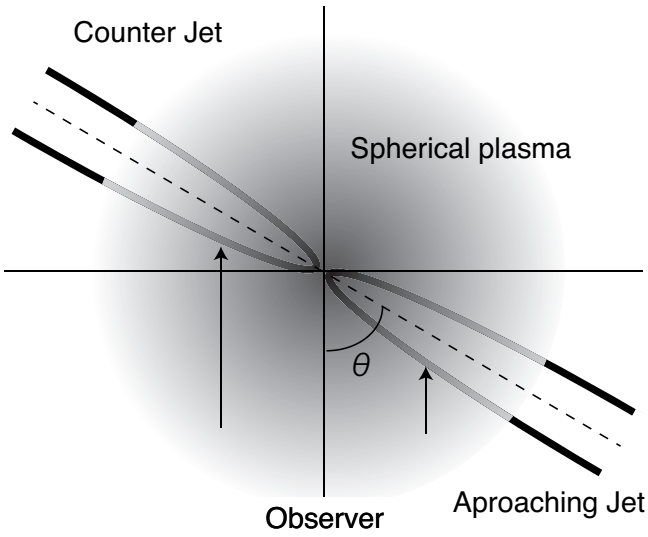

Figure C.2: Schematic of the spherical FFA plasma model of NGC 4261. I discuss in the assumptions that the radial profiles of the electron density and temperature of the plasma are described by power-law functions. The counter jet side is more opaque than the approaching jet side at a given radius from the putative black hole. The arrows show the difference of the path length in the FFA plasma with respect to the observer.

If the electron density and temperature of the FFA plasma follow a power-law function, i.e., $n_{\rm e} = n_0 x^{-s}$ and $T_{\rm e} = T_0 x^{-t}$, the index of the opacity profile, d should be identical in both the approaching and counter sides. When fitting the opacity profile at counter jet side, I fixed d to the same value as that of the approaching jet and obtained τ_0. Table C.1 provided with this fitting result. Let us consider the configuration as shown in Figure C.2. Substituting $n_{\rm e}$ and $T_{\rm e}$ into Equation (A.3), I integrate the path length in the plasma along the line of sight from the jet at $l_0 = \frac{r}{\tan\theta_0}$. The radius x from the black hole is described in (r, l) coordinate as $x^2 = r^2 + l^2$. Therefore, the FFA opacity is given by

$$\tau_{\rm f} = 0.46 n_0^2 T_0^{3/2} \int_{-\infty}^{l_0} (r^2 + l^2)^{-(s-3t/4)} dl, \tag{C.2}$$

By replacing with $l = \frac{r}{\tan\theta}$, I now convert Equation (C.2) into

$$\begin{aligned}
\tau_{\rm f} &= 0.46 n_0^2 T_0^{3/2} \int_0^{\theta_0} \left\{ r^2 \left(1 + \frac{1}{\tan^2\theta} \right) \right\}^{-(s-3t/4)} \frac{r}{\sin^2\theta} d\theta, \\
&= 0.46 n_0^2 T_0^{3/2} r^{-(2s-3t/2-1)} \int_0^{\theta_0} \sin\theta^{2s-3t/2-2} d\theta, \\
&= 0.46 n_0^2 T_0^{3/2} r^{-d} \int_0^{\theta_0} \sin\theta^{d-1} d\theta. \qquad \text{(C.3)} \\
& \qquad \text{(C.4)}
\end{aligned}$$

Adopting $d = 1.55$ from the analysis of the opacity profile (Table C.1), the result of the integration is obtained in numerical calculations. An asymmetric profile of the opacity between both of jets is caused by only the different viewing angles, corresponding to the integration ranges θ_0. Even if n_0 and T_0 are unknown, I can obtain the opacity profile of the counter jet by using the ratio of the opacity to that of the approaching jet.

In this way, I can calculate the FFA core shift profile in the counter jet.

Bibliography

Acciari, V. A., Aliu, E., Arlen, T., et al. 2009, Science, 325, 444

Albert, J., Aliu, E., Anderhub, H., et al. 2007, ApJL, 666, L17

Angel, J. R. P., & Stockman, H. S. 1980, ARAA, 18, 321

Beasley, A. J., & Conway, J. E. 1995, Very Long Baseline Interferometry and the VLBA, 82, 327

Bietenholz, M. F., Bartel, N., & Rupen, M. P. 2004, ApJ, 615, 173

Biretta, J. A., Sparks, W. B., & Macchetto, F. 1999, ApJ, 520, 621

Birkinshaw, M., & Davies, R. L. 1985, ApJ, 291, 32

Blandford, R. D., Königl, A. 1979, ApJ, 232, 34

Blandford, R. D., & Payne, D. G. 1982, MNRAS, 199, 883

Blumenthal, G. R., & Gould, R. J. 1970, Reviews of Modern Physics, 42, 237

Bolton, J. G., Stanley, G. J., & Slee, O. B. 1949, `Nature`, 164, 101

Cannon, R. D., Penston, M. V., & Brett, R. A. 1971, MNRAS, 152, 79

Condon, J. J., & Broderick, J. J. 1988, AJ, 96, 30

Conway, J. E., & Blanco, P. R. 1995, ApJL, 449, L131

Davies, M. L., Franzen, T. M. O., Davies, R. D., et al. 2009, MNRAS, 400, 984

Ferrarese, L., Ford, H. C., & Jaffe, W. 1996, ApJ, 470, 444

Gallimore, J. F., Baum, S. A., & O'Dea, C. P. 1997, `Nature`, 388, 852

Gebhardt, K., & Thomas, J. 2009, ApJ, 700, 1690

Geldzahler, B. J., & Witzel, A. 1981, AJ, 86, 1306

Ghisellini, G., Tavecchio, F., & Chiaberge, M. 2005, A&A, 432, 401

Giroletti, M., Hada, K., Giovannini, G., et al. 2012, A&A, 538, L10

Gliozzi, M., Sambruna, R. M., & Brandt, W. N. 2003, A&A, 408, 949

Greenstein, J. L., & Schmidt, M. 1964, ApJ, 140, 1

Greisen, E. W. 2003, Information Handling in Astronomy - Historical Vistas, 285, 109

Hada, K., Doi, A., Kino, M., et al. 2011, `Nature`, 477, 185

Harris, D. E., Cheung, C. C., Biretta, J. A., et al. 2006, ApJ, 640, 211

Ho, L. C., Rudnick, G., Rix, H.-W., et al. 2000, ApJ, 541, 120

Ho, L. C. 2008, ARAA, 46, 475

Ichimaru, S. 1977, Plasma Physics: Nonlinear Theory and Experiments, 262

Icke, V. 1980, AJ, 85, 329

Jaffe, W., Ford, H. C., Ferrarese, L., van den Bosch, F., & O'Connell, R. W. 1993, `Nature`, 364, 213

Jones, D. L., Wehrle, A. E., Meier, D. L., & Piner, B. G. 2000, ApJ, 534, 165

Jones, D. L., Wehrle, A. E., Piner, B. G., & Meier, D. L. 2001, ApJ, 553, 968

Jorstad, S. G., Marscher, A. P., Mattox, J. R., et al. 2001, ApJS, 134, 181

Jorstad, S. G., Marscher, A. P., Lister, M. L., et al. 2005, AJ, 130, 1418

Junor, W., Biretta, J. A., & Livio, M. 1999, `Nature`, 401, 891

Kaburaki, O., Nankou, T., Tamura, N., & Wajima, K. 2010, PASJ, 62, 1177

Kadler, M., Ros, E., Lobanov, A. P., Falcke, H., & Zensus, J. A. 2004, A&A, 426, 481

Kameno, S., Horiuchi, S., Shen, Z.-Q., et al. 2000, PASJ, 52, 209

Kameno, S., Sawada-Satoh, S., Inoue, M., Shen, Z.-Q., & Wajima, K. 2001, PASJ, 53, 169

Kharb, P., Shastri, P., & Gabuzda, D. C. 2005, ApJL, 632, L69

Koide, S., Shibata, K., Kudoh, T., & Meier, D. L. 2002, Science, 295, 1688

Köonigl, A. 1981, ApJ, 243, 700

Koratkar, A., & Blaes, O. 1999, PASP, 111, 1

Krichbaum, T. P., Alef, W., Witzel, A., et al. 1998, A&A, 329, 873

Lara, L., Alberdi, A., Marcaide, J. M., & Muxlow, T. W. B. 1994, A&A, 285, 393

Lawrence, A. 2005, MNRAS, 363, 57

Lestrade, J.-F., Rogers, A. E. E., Whitney, A. R., et al. 1990, AJ, 99, 1663

Lobanov, A. P. 1998, A&A, 330, 79

Ly, C., Walker, R. C., & Junor, W. 2007, ApJ, 660, 200

Mannucci, A. J., Iijima, B., Sparks, L., et al. 1999, Journal of Atmospheric and Solar-Terrestrial Physics, 61, 1227

Marscher, A. P., Jorstad, S. G., D'Arcangelo, F. D., et al. 2008, `Nature`, 452, 966

Matsumoto, R., & Shibata, K. 1997, IAU Colloq. 163: Accretion Phenomena and Related Outflows, 121, 443

McKinney, J. C. 2006, MNRAS, 368, 1561

Nandra, K., O'Neill, P. M., George, I. M., & Reeves, J. N. 2007, MNRAS, 382, 194

Napier, P. J. 1994, Very High Angular Resolution Imaging, 158, 117

Narayan, R., & Yi, I. 1994, ApJL, 428, L13

Narayan, R., & Yi, I. 1995, ApJ, 452, 710

Nemmen, R. S., Storchi-Bergmann, T., Yuan, F., et al. 2006, ApJ, 643, 652

O'Sullivan, S. P., & Gabuzda, D. C. 2009, MNRAS, 400, 26

Pacholczyk, A. G. 1970, Series of Books in Astronomy and Astrophysics, San Francisco: Freeman, 1970,

Piner, B. G., Jones, D. L., & Wehrle, A. E. 2001, AJ, 122, 2954

Pradel, N., Charlot, P., & Lestrade, J.-F. 2006, A&A, 452, 1099

Pushkarev, A. B., Hovatta, T., Kovalev, Y. Y., et al. 2012, A&A, 545, A113

Qiao, E., Liu, B. F., Panessa, F., & Liu, J. Y. 2013, ApJ, 777, 102

Rybicki, G. B., & Lightman, A. P. 1979, New York, Wiley-Interscience, 1979. 393 p.,

Salpeter, E. E. 1964, ApJ, 140, 796

Seyfert, C. K. 1943, ApJ, 97, 28

Shakura, N. I., & Sunyaev, R. A. 1973, A&A, 24, 337

Shepherd, M. C., Pearson, T. J., & Taylor, G. B. 1994, BAAS, 26, 987

Shibata, K., & Uchida, Y. 1990, PASJ, 42, 39

Sokolovsky, K. V., Kovalev, Y. Y., Pushkarev, A. B., & Lobanov, A. P. 2011, A&A, 532, A38

Taam, R. E., Liu, B. F., Yuan, W., & Qiao, E. 2012, ApJ, 759, 65

Thompson, A. R., Clark, B. G., Wade, C. M., & Napier, P. J. 1980, ApJS, 44, 151

Thompson, A. R., Moran, J. M., & Swenson, G. W., Jr. 2001, "Interferometry and synthesis in radio astronomy by A. Richard Thompson, James M. Moran, and George W. Swenson, Jr. 2nd ed. New York

Tingay, S. J., & Murphy, D. W. 2001, ApJ, 546, 210

Tonry, J. L., Blakeslee, J. P., Ajhar, E. A., & Dressler, A. 2000, ApJ, 530, 625

Treuhaft, R. N. & Lanyi, G. E., 1987, Radio Sci. 22, 251

Urry, C. M., Padovani, P., & Stickel, M. 1991, ApJ, 382, 501

Vermeulen, R. C., Readhead, A. C. S., & Backer, D. C. 1994, ApJL, 430, L41

Visvanathan, N. 1969, ApJL, 155, L133

Walker, R. C., Romney, J. D., & Benson, J. M. 1994, ApJL, 430, L45

Woo, J.-H., & Urry, C. M. 2002, ApJ, 579, 530

Yuan, F., Quataert, E., & Narayan, R. 2003, ApJ, 598, 301

Acknowledgment

I owe this thesis to many people on supports, suggestions and helps.

Firstly, I am very grateful for Yasuhiro Murata, my supervisor, who has guided and encouraged me to write this doctor thesis. I feel myself fortunate to be given his valuable advice and knowledge about astrophysics. I wish to acknowledge to Akihiro Doi, who taught me principles of techniques on data analysis and provided much advice throughout writing of this thesis. I have learned a lot of things from his strict attitude for deriving and treating scientific result. Many thanks for collaborators, especially Hiroshi sudou, who provided me opportunities to analysis data, Seiji Kameno, who gave me helpful comments, and Kazuhiro Hada, who taught and discussed me regarding with core shifts. And I would like to thank colleagues and friends, Kozue Kusuno, Keiko, Matsuta, Koji Tanaka, Gen Kato, and members of kimission and kimission FC. A little discussion and a lot of trivial talk with them is precious memory for my life. Finally, I would acknowledge my father, mother and sister for their great help. The support of my mind when I seem to fail is always their kindness and tenderness.